Main Manuscript for

Zinc is a Key Regulator of the Sperm-Specific K^+ Channel (Slo3) Function

Authors

Rizki Tsari Andriani[1,2], Tanadet Pipatpolkai[3], Haruhiko Miyata[4], Masahito Ikawa[4], Yasushi Okamura[1,5], Takafumi Kawai[1,6*]

Affiliations

1 Department of Physiology, Graduate School of Medicine, Osaka University, Suita, Japan

2 Graduate School of Medicine, Osaka University JSPS International Research Fellow

3 School of Physical and Mathematical Science, Nanyang Technological University, Singapore

4 Research Institute for Microbial Diseases, Osaka University, Suita, Japan

5 Graduate School of Frontier Bioscience, Osaka University, Suita, Japan

6 Department of Molecular and Cellular Physiology, Graduate School of Medicine, Ehime University, Ehime, 791-0295, Japan

***Corresponding author:**

Takafumi Kawai

Department of Molecular and Cellular Physiology, Graduate School of Medicine, Ehime University, Ehime, 791-0295, Japan

Phone: +81-89-960-5241

FAX: +81-89-960-5242

Email: kawai.takafumi.ra@ehime-u.ac.jp

Keywords: Slo3, zinc, voltage-gated potassium channel, sperm, capacitation.

Abstract

The voltage- and pH-gated Slo3 potassium channel is exclusively expressed in mammalian spermatozoa. Its sensitivity to both voltage and alkalization plays a crucial role in sperm fertility, which is tightly coupled to the capacitation process. Here we show that sperm-enriched divalent cation Zn^{2+} undergoes dynamic alteration in spermatozoa during capacitation. We also found that intracellular Zn^{2+} regulates alkalinization-induced hyperpolarization in mouse spermatozoa which is mediated by Slo3 channel. Further examination of zinc regulation in mouse Slo3 (mSlo3) revealed that, in *Xenopus* oocyte expression system, intracellular zinc directly inhibits mouse Slo3 currents in dose-dependent manner at micromolar concentrations, with exceptionally slow dissociation. By combining MD simulations and electrophysiology, we also identified amino acid residues contributing to the Zn^{2+} slow dissociation from Slo3 channels. Our studies uncover the importance of intracellular zinc dynamics and its regulatory role in ion channels during sperm capacitation.

Main Text

Introduction

Zinc is an essential metal ion involved in numerous biological functions, including as a regulatory component to various proteins such as enzymes, transcription factors, and ion channels (Fayyazuddin et al., 2000; Gao et al., 2017; Maret, 2013; Sun et al., 2007; Vallee & Falchuk, 1993; Zheng et al., 2001). In the reproductive system, spermatozoa is a type of cell that is known to have high intracellular zinc content, which influences its production, maturation, and physiological functions (Chia et al., 2000; Fallah et al., 2018; Henkel et al., 1999; Riffo et al., 1992; Yamaguchi et al., 2009). Zinc is also present in the seminal fluid at high concentrations (~1-1.5 mM) (Henkel et al., 1999; Riffo et al., 1992), and extensive studies have elucidated their role in regulating sperm physiology. For instance, extracellular zinc has been shown to influence human sperm motility, which negatively correlates with the concentration (Henkel et al., 1999, 2005). Another study also suggested that increased zinc concentration inhibits sperm motility (Riffo et al., 1992). Despite considerable evidence that sperm motility is regulated by extracellular zinc, intracellular zinc has also been implicated in playing a regulatory role. One study demonstrated that chelating intracellular zinc reduces sperm motility and velocity (Sørensen et al., 1999). However, the underlying mechanism by which zinc regulates sperm motility remains unclear.

During fertilization, spermatozoa undergo capacitation, a series of physiological processes that determine the success of fertilizing the egg within the female reproductive tract (Austin, 1951; Chang, 1951). This capacitation involves the changes of activities in various ion channels, which leads to diverse physiological changes, such as pH, calcium level, and membrane potential (Arnoult et al., 1999; Breitbart, 2002; Publicover et al., 2007; Vredenburgh-Wilberg & Parrish, 1995; Y. Zeng et al., 1995, 1996). Moreover, recent studies have shown that the activity of ion channels is regulated by zinc. Indeed, extracellular zinc has been shown to inhibit the flagellar voltage-gated proton channel Hv1, which is supposed to control intracellular pH in human sperm (Grahn et al., 2023; Lishko

67 et al., 2010; Zhao et al., 2018). Thus, it is possible that the high levels of zinc in
68 spermatozoa regulates their physiological properties.

69 In the present study, we find that intracellular zinc is exported during capacitation,
70 indicating that zinc dynamics in spermatozoa play an important role in fertilization.
71 Furthermore, zinc significantly inhibited the alkalinization-induced hyperpolarization in
72 mouse sperm, which is mediated by Slo3 ($K_{Ca}5.1$), a sperm specific pH- and voltage-gated
73 potassium channel (Schreiber et al., 1998; X. Zhang et al., 2006).

74 We further discovered that intracellular zinc directly inhibits mouse Slo3 (mSlo3) currents
75 using *Xenopus* oocytes. Of note, this inhibition is pH-dependent, voltage-dependent and
76 has a long-lasting inhibitory effect even after the washout. Coexpression of mSlo3 with the
77 auxiliary subunit Lrrc52, to mimic the native environment (Yang et al., 2011; X. H. Zeng
78 et al., 2015), consistently demonstrates zinc's inhibitory effect. Additionally, we identify
79 potential key amino acids in the mSlo3 channel that serve as the zinc binding site. Our
80 findings highlight the importance of intracellular zinc dynamics and its regulatory role over
81 ion channels during capacitation in spermatozoa.

82 **Results**

83 **Intracellular zinc is exported from sperm during capacitation.**

84 To investigate the role of intracellular zinc during capacitation, we monitored the
85 intracellular zinc concentration utilizing the zinc-sensitive fluorophore FluoZin3-AM.
86 Fluorescence signals were successfully detected in both the head and flagellum of isolated
87 mouse spermatozoa (Fig. 1A). As expected, the head of the spermatozoa showed a stronger
88 fluorescence signal compared to the flagellum, likely due to its higher zinc capacity. We
89 also treated spermatozoa with Toyoda, Yokoyama, Hoshi (TYH) medium (Toyoda et al.,
90 1971), which is well established capacitation-inducing medium *in vitro*. We observed that
91 there was a gradual and significant decrease in fluorescence intensity in both regions (Fig.
92 1B), particularly prominent in the flagellum (Fig. 1C). This decline suggests the active
93 release of intracellular zinc from sperm flagellum occurs during capacitation. In contrast,

94 the fluorescence intensity of the control group of non-capacitated sperm remained
95 unchanged (Fig. 1B).

96 Additionally, we examined the effect of intracellular zinc on sperm motility before and
97 after capacitation (Fig. 1—figure supplement 1A-E). We incubated the isolated
98 spermatozoa with cell permeable Zn^{2+} chelator N,N,N',N'-Tetrakis(2-
99 pyridylmethyl)ethylenediamine (TPEN) and measured the motility parameters before and
100 after capacitation. We found that VAP (average path velocity), VCL (curvilinear velocity),
101 and VSL (straight-line velocity) were influenced by the TPEN treatment only after the
102 capacitation, as shown in Fig. 1—figure supplement 1. These results demonstrate that the
103 dynamics of zinc levels during capacitation potentially contributes to sperm motility,
104 highlighting the importance of zinc action in sperm physiology.

105 **Intracellular zinc inhibits the alkalinization-induced hyperpolarization in sperm**

106 It is already known that sperm capacitation is well associated with the increase of
107 intracellular pH (Vredenburgh-Wilberg & Parrish, 1995; Y. Zeng et al., 1996), which leads
108 to the hyperpolarization of the membrane (Arnoult et al., 1999; Y. Zeng et al., 1995) as
109 well as the elevation of intracellular Ca^{2+} concentration level (Breitbart, 2002; Publicover
110 et al., 2007) through diverse ion channel activities. To explore whether these pathways are
111 influenced by intracellular zinc, we used perforated patch-clamp techniques. It has been
112 reported that under the whole-cell current clamp of mouse epididymal spermatozoa, resting
113 membrane potential (Vm) is hyperpolarized after intracellular alkalinization (Navarro et
114 al., 2007). Therefore, we applied 10 mM NH_4Cl, which is routinely used to alkalize
115 intracellular pH (Madshus, 1988), to spermatozoa. As expected, we observed that it
116 hyperpolarized the membrane by -17.37 ± 7.09 mV; n=6 (Fig. 1E, G). Then, we applied 10
117 mM NH_4Cl with 100 μM zinc pyrithione (ZnPy), a zinc ionophore. In contrast to the
118 control group, there was no remarkable hyperpolarization in the presence of ZnPy as the
119 ΔVm was 0.99 ± 6.17 mV; n=3 (Fig. 1F, G). These findings indicate that either
120 extracellular or intracellular zinc inhibits the alkalinization-induced hyperpolarization in
121 mouse sperm.

122 To examine the possibility that intracellular, but not extracellular, zinc is responsible for
123 inhibiting the alkalinization-induced hyperpolarization, we measured membrane potential
124 of sperm using the patch-clamp technique in conventional whole-cell configuration with
125 pH_i = 6.0 (Fig. 1H). In the test group, the patch pipette contained 100 μM $ZnCl_2$ (Fig. 1J),
126 while the control group did not (Fig. 1I). Consistent with the perforated patch-clamp
127 results, we observed alkalinization-induced hyperpolarization upon applying NH_4Cl in the
128 control (ΔVm= -24.12 ± 13.16 mV; n=5; Fig. 1I, K). In contrast, alkalinization-induced
129 hyperpolarization was reduced in the 100 μM $ZnCl_2$ group (ΔVm= -6.80 ± 2.35 mV; n=4;
130 Fig. 1J, K).

131 We also measured Slo3 current using perforated patch-clamp recordings in spermatozoa
132 treated with ZnPy, before and after the addition of NH_4Cl. Control experiments were
133 conducted in the absence of ZnPy, in which Slo3 current were recorded before and after
134 the application of 10 mM NH_4Cl (Fig. 1L-N; Fig. 1—figure supplement 2A, B). Slo3
135 current in sperm tended to be inhibited by zinc, as shown by the plot of absolute Slo3
136 current after the addition of 10 mM NH_4Cl in the absence of ZnPy (control) and in the
137 presence of 100 μM ZnPy (Fig. 1L, M). There was a decrease in the fold change calculated
138 from the absolute current before and after the addition of 10 mM NH_4Cl of ZnPy treated
139 group (1.4 ± 0.56; n=4) compared to the control group (2.39 ± 0.55; n=4; Fig. 1N). Taken
140 together, these results confirmed that intracellular zinc indeed inhibits alkalinization-
141 induced hyperpolarization in mouse sperm.

142 **Zinc inhibits mouse Slo3 (mSlo3) current.**

143 Our findings suggest that intracellular zinc inhibits a key process in sperm capacitation,
144 specifically the alkalinization-induced hyperpolarization. Previous studies have identified
145 the pH-and voltage-dependent potassium channel Slo3 is responsible for the principal K^+
146 current (I_{KSper}) in mouse spermatozoa (Navarro et al., 2007; Santi et al., 2010; Schreiber et
147 al., 1998; X. H. Zeng et al., 2011). During capacitation, the rise in pHi leads to the
148 activation of Slo3 channels, resulting in membrane hyperpolarization (Santi et al., 2010).
149 Given this context, we next investigated whether intracellular zinc acts directly on the Slo3
150 channel.

151 We expressed the mSlo3 channel in the *Xenopus* oocyte expression system and conducted
152 inside-out patch-clamp recordings. The bath solution was initially set to pH 8.0, and
153 recordings were performed using a high-speed perfusion system. A ramp pulse from -100
154 mV to + 100 mV with a holding potential of -60 mV was applied. We observed a robust
155 pH- and voltage-dependent mSlo3 current at pH 8.0 (Fig. 2A, B), consistent with previous
156 reports (Leonetti et al., 2012; Schreiber et al., 1998; X. Zhang et al., 2006). The application
157 of 100 μM of $ZnCl_2$ resulted in the inhibition of 36.62 ± 11.65 % (n=6) of mSlo3 current
158 (Fig. 2A, B). Of note, the inhibited mSlo3 current by zinc was never restored after the wash
159 out of zinc even for more than 30 seconds. However, when pH 6.0 was applied to
160 completely abolish the mSlo3 current, followed by the application of pH 8.0, the mSlo3
161 current recovered (Fig. 2A, B). We also determined the IC_{50} of zinc inhibition by applying
162 zinc at concentrations 0.1, 1, 10, 100, and 1000 μM for 30 seconds. The dose-response
163 curve, fitted to the Hill equation with a standard slope (Hill slope of -1.0), yielded an IC_{50}
164 = 145.2 μM (Fig. 2C).

165 We also tested the effect of zinc at a lower pH of 7.5. We observed the pH- and voltage-
166 dependent mSlo3 current at this pH. However, the 100 μM of $ZnCl_2$ application did not
167 affect the mSlo3 current (Fig. 2D-F). To rule out instrumental and human error, we also
168 tested the effect of pH 6.0 which suppresses Slo3 activity. As expected, the application of
169 pH 6.0 completely inhibited the mSlo3 current, and the subsequent application of pH 7.5
170 restored the current (Fig. 2D-F).

171 We also conducted step pulse protocols from -100 mV to +180 mV with a holding potential
172 of -60 mV to assess whether zinc inhibition is voltage-dependent. At pH 8.0, we observed
173 a robust mSlo3 current, which was inhibited by 100 μM $ZnCl_2$ (Fig. 2G, H). The current-
174 voltage (I-V) relationship indicated voltage-dependent zinc inhibition (Fig. 2H). The ratio
175 of I_{zinc} to $I_{control}$ plotted against membrane potential also demonstrated that zinc inhibition
176 of mSlo3 current is voltage-dependent (Fig. 2—figure supplement 1B).

177 In addition, we plotted the conductance-voltage (G-V) relationship by calculating the
178 conductance from the maximum current amplitude at steady-state, as the tail current
179 recordings of mSlo3 were unsuccessful. We noted that V_{50} of mSlo3 current shifted to more

180 hyperpolarized potentials in the presence of zinc (V_{50} control = 80.67 ± 2.32; V_{50} zinc =
181 49.68 ± 1.38; n=13; Fig. 2—figure supplement 1C).

182 As we observed the long-lasting inhibitory effect of zinc on mSlo3 current, we examined
183 whether a zinc chelator could restore the mSlo3 current to the baseline level without
184 applying acidic pH. We used 5 mM EGTA, a divalent cation chelator which strongly
185 chelates zinc ($Kd_{(Zn)}$ ~1 nM) (Hu et al., 2009). Zinc-inhibited mSlo3 current could not be
186 recovered by pH 8.0 alone (Fig. 2I). However, significant current recovery was observed
187 when 5 mM EGTA was included in the pH 8.0 bath solution (Fig. 2J). Specifically, 5 mM
188 EGTA recovered 49.22 ± 37.98 % of the mSlo3 current (n=5), compared to pH 8.0 alone,
189 which showed no significant recovery (5.62 ± 24.4 %; n= 7), as shown in Fig. 2K.

190 Additionally, we investigated the presence of endogenous zinc in Slo3 by perfusing pH 8.0
191 followed by 5 mM EGTA at the beginning of the recording to detect any changes in the
192 baseline current. The baseline current showed a slight increase upon perfusion with 5 mM
193 EGTA, indicating the presence of endogenous zinc affecting the baseline current in Slo3
194 (Fig. 2—figure supplement 1D, E).

195 Taken together, these results showed that zinc has a long-lasting inhibitory effect on mSlo3
196 current that cannot be reversed by pH 8.0 alone. The inhibitory effect is pH-dependent, as
197 complete inhibition at pH 6.0 followed by recovery at pH 8.0 was observed. In addition,
198 zinc inhibition is voltage-dependent, and the application of 5 mM EGTA, which strongly
199 chelates zinc, can partially recover mSlo3 current.

200 **Zinc more efficiently inhibits mSlo3 current when coexpressed with the auxiliary**
201 **subunit Lrrc52**

202 In its native environment of spermatozoa, Slo3 is expressed with its auxiliary subunit
203 Lrrc52 (Yang et al., 2011; X. H. Zeng et al., 2015). Lrrc52 shifts the Slo3 gating to more
204 negative potentials, making the channel easier to open (Yang et al., 2011). We coexpressed
205 mSlo3 with mouse Lrrc52 (mLrrc52) in the *Xenopus* expression system to perform inside-
206 out patch clamp recordings.

207 The mSlo3+mLrrc52 current was observed upon the application of pH 8.0. A ramp pulse
208 protocol from -100 mV to +100 mV was applied with a holding potential of 0 mV. Similar
209 to mSlo3 alone, in the presence of mLrrc52, mSlo3 current was also inhibited by 100 μM
210 $ZnCl_2$ (Fig. 3A, B). In addition, zinc inhibition was not recovered after washing with the
211 zinc-free solution (Fig. 3B). A significant leftward shift in IC_{50} was observed when the
212 dose-response curve was plotted for coexpression with mLrrc52 (Fig. 3C; IC_{50} = 15.2 μM;
213 n= 3-8) compared to mSlo3 alone (Fig. 2C, Fig. 3C).

214 Additionally, when pH 7.5 was applied to depolarized potentials, mSlo3+mLrrc52 current
215 was activated and in contrast with mSlo3 alone (Fig. 2D-F), 100 μM $ZnCl_2$ already
216 inhibited mSlo3+mLrrc52 current at pH 7.5 (Fig. 3D, E, Fig. 3—figure supplement 1D).
217 Alkalinization appeared to increase the percentage of current inhibition by 100 μM $ZnCl_2$
218 (Fig. 3F; pH 7.5 = 32.51 ± 8.62 %; n=3 and pH 8.0 = 52.61 ± 8.23 %; n=8).

219 We next conducted recordings using a step pulse protocol from -100 mV to +180 mV with
220 a holding potential of -60 mV. Upon applying pH 8.0, we observed a significant
221 mSlo3+mLrrc52 current, which was inhibited by 100 μM $ZnCl_2$ (Fig. 3—figure
222 supplement 1A, B). Again, the I-V relationship confirmed that zinc inhibition was voltage-
223 dependent (Fig. 3—figure supplement 1B). V_{50} of mSlo3+mLrrc52 current was also shifted
224 into more hyperpolarized potentials in the presence of zinc (V_{50} control = 72.93 ± 2.06 V_{50}
225 zinc = 56.27 ± 2.75; n=13; Fig. 3—figure supplement 1C).

226 Taken together, when co-expressed with mLrrc52, mSlo3 current was more efficiently
227 inhibited by zinc.

228 **E169 and E205 located within VSD are important for the sustained zinc inhibition of**
229 **mSlo3 current**

230 To elucidate the mechanism of zinc inhibition on the mSlo3 channel, we aimed to identify
231 the structural determinants required for this inhibition using a range of computational tools
232 and mutagenesis. First, we used the AlphaFold3 structure prediction webserver (Abramson
233 et al., 2024) to predict the zinc binding site on the mSlo3 channel. Notably, the prediction
234 has shown that the majority of the zinc binding sites are located in the channel's

235 intracellular regulator of K^+ conductance (RCK) domain, which consists of RCK1 and
236 RCK2, with very few zinc sites in the transmembrane domain (Fig. 4—figure supplement
237 1A). The RCK domain is also recognized as crucial for zinc binding in Slo channel families
238 (Hou et al., 2010; J. Zhang et al., 2023).

239 To validate the site within the intracellular region, we conducted site-directed mutagenesis
240 on intracellular domain focusing on RCK1, RCK1/RCK2 linker, and RCK2 (H354R,
241 H383R, H423R, H516R, H564R, H606A, H695R, and H720R) to assess changes in
242 channel sensitivity to zinc. However, the percentage of current inhibition varied across the
243 mutated constructs, showing either increases or no appreciable change (Fig. 4—figure
244 supplement 1B, C). We also generated a chimera where RCK2 of mSlo3 was replaced with
245 RCK2 from mSlo1, but this chimera exhibited slightly increased sensitivity to zinc (Fig.
246 4—figure supplement 1B, C). Taken together, this concludes that, unlike Slo1, the zinc
247 binding site is unlikely to be located in the RCK or the intracellular domain of the channel.

248 We then diverge our focus to the intracellular site of the channel. Given that zinc has been
249 shown to shift the G-V relationship of the mSlo3 channel and its complex with Lrrc52 (Fig.
250 2—figure supplement 1C, Fig. 3—figure supplement 1C), we suspect that the binding site
251 is more likely to be located in the transmembrane (TM) region. To enhance the prediction
252 within the transmembrane segment, we computationally truncated the intracellular domain,
253 allowing a key binding site to be found near E169 and E205 within the voltage-sensing
254 domain (VSD) with the AlphaFold3 structure prediction webserver (Fig. 4A). Next, we
255 conducted triplicates of 200 ns molecular dynamics simulations of the AlphaFold3 full-
256 length Slo3 tetrameric structure to validate this binding site where the Slo3 channel is
257 solvated in 0.15 M $ZnCl_2$ and 0.15 M KCl (Fig. 4B). Here, we show that using MD
258 simulations, a similar zinc site is also observed near E169 and E205, validating the
259 prediction results by AlphaFold3 (Fig. 4C). In addition, we also observed another zinc
260 binding near the pore at E310 and E313 (Fig. 5—figure supplement 1A).

261 To test the stability of zinc within E169 and E205, we removed all the $ZnCl_2$ in the
262 simulation box, leaving just 4 zinc ions near E169 residues and conducted three separate
263 simulations for 200 ns, leading to 12 data points. Our simulations show that zinc remains

264 stable, with the low root mean square deviation (RMSD) within its binding site in the
265 transmembrane region, validating the stability within its binding site (Fig. 4D).

266 To validate the binding site further, we conducted a computational site-directed
267 mutagenesis to further assess zinc stability after the mutation of the nearby acidic residue,
268 E169A and E205A. Here, we show that the RMSD of the E169A mutant increases more
269 than WT and E205A (Fig. 4E). Together, our simulation suggested that E169 and E205 are
270 indeed important for the binding of zinc by Slo3.

271 We then examined zinc sensitivities of mSlo3 currents from oocytes expressing mutants
272 by electrophysiology with mutation of zinc binding residues on the mSlo3 channel
273 predicted by MD simulations, which is located in the S2-S3 linker (D162), S3 domain
274 (E169), S4 domain (E205) and the intracellular linker between TM and RCK1 (E326) (Fig.
275 4C-E, Fig. 5A, Fig. 5—figure supplement 1B). All of these mutants exhibited similar
276 current inhibition by zinc compared to wildtype (WT = 29.58 ± 11.84 %, n=7; D162S =
277 19.85 ± 11.63 %, n=3; E169A = 44.17 ± 20.27 %, n=4; E205 = 33.08 ± 10.28 %, n=4;
278 E326 = 27.54 ± 1.27 %, n=2; Fig. 5B, C, Fig. 5—figure supplement 1C, D).

279 On the other hand, when we analyzed the percentage of current recovery of all the mutants,
280 E169A and E205A showed significant current recovery upon the wash-out by pH 8.0 alone
281 (WT = 5.62 ± 24.40 %, n=7; D162S = 0.86 ± 37.60 %, n = 3; E169A = 48.74 ± 31.61 %,
282 n=4; E205A = 48.65 ± 14.37 %, n=4; E326 = -3.27 ± 1.43 %, n=2; Fig. 5B, D, Fig. 5—
283 figure supplement 1C, E). Additionally, we performed sequence alignment by using
284 ClustalO between mSlo3, mSlo1, and mSlo2.2. It is worth noting that only human and frog
285 variants of Slo2.1 sequence are available in the database, so we included only Slo2.2
286 subtype, as our focus was on Slo3 in mouse sperm. Based on the alignment, E169 (mSlo3
287 numbering) is conserved among the Slo family channels in mice, while in contrast E205
288 (mSlo3 numbering) is not (Figure 5 – supplementary figure 1F).

289 Taken together, consistent with MD simulation results, our electrophysiological recordings
290 demonstrated that the long-lasting inhibitory effect of zinc was partly abolished by these
291 mutations. Thus, our findings highlight the contribution of E169A in the bottom of S3

292 domain and E205A in the bottom of S4 domain in zinc-mediated inhibition of mSlo3
293 current.

294

295 **Zinc alters the dynamics of VSD motion in mSlo3**

296 Given the observed zinc-induced shift in the G-V relationship of both mSlo3 and
297 mSlo3+mLrrc52, along with MD simulations and mutagenesis data, it is likely that VSD
298 is involved in zinc inhibition of mSlo3. Then, we performed voltage-clamp fluorometry
299 (VCF) experiments to track the motion of the VSD in the presence and absence of zinc.
300 First, to identify suitable site for labeling with TMRM, we performed VCF scanning by
301 introducing Cys mutations one at a time at the top of S3, S3-S4 linker, and the top of S4 of
302 mSlo3 VCF construct (Fig. 6—figure supplement 1A). Two native, extracellular cysteines
303 were mutated to avoid non-specific labeling (mSLo3 C19S/C131S) and the desired Cys
304 mutations were then added on this double-mutant background. Initial scanning of VCF
305 constructs L188C, K189C, S190C, and N191C (Fig. 6—figure supplement 1A-E)
306 conjugated with TMRM resulted in no detectable fluorescence intensity (F) changes (ΔF).
307 Subsequently, we coexpressed the mSlo3 VCF constructs with mLrrc52 to increase the
308 level of mSlo3 expression in heterologous expression system (Leonetti et al., 2012). Out
309 of three mutants coexpressed with mLrrc52 (L193C, G194C, and L195C; Fig. 6—figure
310 supplement 1F-H), L193C, which is located in the top of S4 domain, produced fluorescence
311 intensity changes in response to voltage steps (Fig. 6—figure supplement 1F) (ΔF/F= 1.15
312 ± 0.48 %; n=4).

313 We next performed VCF recordings in the absence and presence of zinc. Oocytes were
314 held at -60 mV and the step pulses were applied from -160 mV to + 160 mV. Fluorescence
315 change could be observed in response to voltage steps ($\Delta F/F_{Control}$ = 2.84 ± 1.25 % at +160
316 mV; n=7; Fig. 6A). A puff of 10 mM zinc solution was then manually injected into the
317 same oocyte using a glass needle with positive pressure. 60 seconds post-injection, a
318 second set of step pulses was applied to record the response under zinc application ($\Delta F/F_{Zinc}$
319 = 2.53 ± 1.37 % at +160 mV; n=7; Fig. 6A). In the presence of zinc, the V_{50} of fluorescence-

320 voltage (F-V) relationship was shifted into more depolarized potentials (V_{50} control = -
321 21.68 ± 3.04; V_{50} zinc = 27.04 ± 1.05; Fig. 6B). This decrease in ΔF/F was more
322 pronounced at certain voltages, such as 0 mV (Fig. 6E-F), and extended up to +80 mV. I-
323 V relationship (Fig. 6C) showed that mSlo3 current was inhibited by zinc, consistent with
324 what has been observed in the patch-clamp recordings (Fig. 2 and Fig. 3). Consistent with
325 F-V relationship, the conductance-voltage (G-V) was also shifted into more depolarized
326 potentials (V_{50} control = 21.11 ± 4.8; V_{50} zinc = 38.62 ± 28.8; Fig. 6D). Collectively, these
327 results clearly indicate that the VSD motion of mSlo3 is influenced by the application of
328 intracellular zinc.

329

330 **Discussion**

331 The present study aims to understand the roles of intracellular zinc in sperm physiology,
332 focusing on sperm capacitation. Our results demonstrated that intracellular zinc is exported
333 from spermatozoa during capacitation. We further discovered that intracellular zinc
334 regulates alkalinization-induced hyperpolarization in mouse spermatozoa, mediated by
335 Slo3 channel. Detailed analysis of zinc's regulatory effects mSlo3 in the *Xenopus* oocyte
336 expression system revealed that intracellular zinc directly inhibits mSlo3 currents with
337 exceptionally slow dissociation. By combining MD simulations and electrophysiology, we
338 identified amino acid residues important for zinc-mediated inhibition of Slo3 activities.

339 **Zinc levels are dynamic during capacitation**

340 Using FluoZin3-AM for zinc imaging, we confirmed the presence of intracellular zinc in
341 sperm (Fig. 1A), which is consistent with previous findings (Henkel et al., 1999). Our
342 observations revealed that treatment with capacitation medium induced a decrease in zinc
343 fluorescence intensity (Fig. 1B, C), suggesting that zinc levels are dynamic during
344 capacitation. Previous studies using boar, bull and human spermatozoa have identified four
345 distinct patterns of zinc localization associated with the state of capacitation (Kerns et al.,
346 2018). In non-capacitated sperm, high concentration of zinc is present throughout the
347 whole sperm from the sperm head to the whole sperm-tail, and the subcellular zinc

348 localization shifts to a medium level in both the sperm head and the sperm tail mid piece
349 (Kerns et al., 2018). In congruent with this, our findings also demonstrated a decrease in
350 fluorescence intensity in both the head and flagellum of mouse spermatozoa during
351 capacitation (Fig. 1B, C). These results suggest that zinc dynamics appear to play an
352 important role in sperm capacitation.

353 Indeed, we observed that zinc chelator significantly affected the sperm motility specifically
354 in VAP (average path velocity), VCL (curvilinear velocity), and VSL (straight-line
355 velocity) only after, but not before, capacitation (Fig. 1—figure supplement 1). Of note, it
356 has been recently reported that all these motility parameters (VAP, VCL, and VSL) are
357 reduced by Slo3-specific inhibitors in human sperm (M. Lyon et al., 2023). These findings
358 are consistent with the idea that endogenous zinc dynamics control sperm motility through
359 Slo3 during the capacitation process.

360 The identity of the transporters directly responsible for zinc dynamics remains unclear. To
361 maintain zinc homeostasis, two protein families facilitate the transport of Zn^{2+} across
362 cellular and intracellular membranes in opposite directions: zinc transporter proteins (ZnT)
363 and Zrt-, Irt-like proteins (ZIP) (Kambe et al., 2004). ZIP12 has been reported to be highly
364 expressed in mouse testis (Zhu et al., 2022), as well as ZnT-1 (Elgazar et al., 2005). The
365 mechanisms of zinc transport in sperm during capacitation remains a subject to be
366 investigated in future studies.

367 **Intracellular zinc directly inhibits mSlo3 channels**

368 Our findings from inside-out patch-clamp recordings indicate that zinc directly inhibits
369 mSlo3 channels in a dose-dependent manner (Fig. 2). Zinc inhibition in mSlo3 channels is
370 dependent on pH (Fig. 2A-E), voltage (Fig. 2G-H; Fig.2—figure supplement 1B, C) and
371 exhibits a long-lasting inhibitory effect (Fig. 2I, K). This sustained inhibitory effect of zinc
372 can be partially restored by EGTA, a divalent ion chelator with high affinity for zinc (Fig.
373 2J, K; Fig.2—figure supplement 1D, E). Previous studies indicate that zinc also regulates
374 the Slo channel family, albeit with varying effects among Slo3 channel subtypes: zinc
375 activates Slo1 channels (Hou et al., 2010) while inhibiting Slo2.2 channels (Budelli et al.,

376 2016; J. Zhang et al., 2023). Zinc may produce these opposite effects on Slo2.2 and Slo1
377 by binding to distinct, non-conserved sites among the subtypes (J. Zhang et al., 2023).

378 Zinc inhibition on mSlo3 channels is characterized by the slow dissociation of zinc from
379 the channel (Fig. 2I-K). Similar slow dissociation has been observed in zinc-regulated ion
380 channels and receptors, such as NMDA and glycine receptors (Paoletti et al., 1997;
381 Trombley et al., 2011). In NMDA receptors, high zinc affinity results in slow dissociation,
382 which has been suggested to have a physiological relevance in neurons (Paoletti et al.,
383 1997).

384 Slow dissociation typically indicates high-affinity binding. In contrast to NMDA receptors,
385 which exhibit IC_{50} values ranging from nM to μM, mSlo3 has a relatively high IC_{50} for
386 zinc inhibition (145.2 μM). This might be due to the ~40-second zinc application time in
387 our study, which may have been insufficient to fully observe the effects at lower
388 concentrations (Fig. 2B, C). Extended exposure of intracellular zinc in sperm could
389 potentially result in greater inhibition.

390 Furthermore, our results also show that when mSlo3 is coexpressed with Lrrc52 the lower
391 concentration of zinc was sufficient to inhibit mSlo3 channels (Fig. 3). Although we still
392 did not identify the exact mechanism underlying it, Lrrc52 shifts the gating of mSlo3 to
393 more hyperpolarized potentials and lower pH, making the channel easier to open (Leonetti
394 et al., 2012; Yang et al., 2011; X. H. Zeng et al., 2015). Considering that the zinc inhibition
395 of Slo3 depends on membrane potential and intracellular pH, it is understandable that the
396 presence of this auxiliary subunit would lead to more efficient inhibition by zinc.

397

398 **Structural determinants of zinc inhibition in the mSlo3 channel**

399 We identified potential key amino acids in the mSlo3 channel that may serve as zinc
400 binding sites using MD simulations and amino acid mutagenesis (Fig. 4, 5; Fig. 4—figure
401 supplement 1, Fig. 5—figure supplement 1). Previous studies on the Slo channel family
402 indicates that zinc binding sites are located in RCK1 domain for Slo1 (Hou et al., 2010)

403 and RCK2 domain for Slo2.2 (J. Zhang et al., 2023). However, in mSlo3 channel, our
404 results didn't show that either RCK1 or RCK2 may serve as zinc binding site (Fig. 4—
405 figure supplement 1).

406 On the other hand, our analysis of current recovery for mSlo3 mutants in the VSD region
407 revealed that E169A and E205A showed significant recovery upon wash-out with pH 8.0.
408 This result aligns with MD simulations showing faster zinc dissociation for both E169A
409 and E205A, indicating their contributions in zinc-mediated inhibition. Thus, the cluster of
410 negative residues within the VSD serve as the zinc binding site in the mSlo3 channel.

411 Based on sequence alignment, E169 (mSlo3 numbering) is conserved among Slo family
412 channels in mice, whereas E205 (mSlo3 numbering) is not (Fig. 5—figure supplement 1F).
413 To date, no studies have examined the corresponding residues to E169 (E191 in mSlo1 or
414 E176 in mSlo2.2) for their potential zinc sensitivity, likely because the established zinc
415 binding sites in these channels are located in the RCK1 domain for Slo1 (Hou et al., 2010)
416 and the RCK2 domain for Slo2.2 (J. Zhang et al., 2023). The identified zinc binding site in
417 Slo2.2 is conserved in Slo2.1 but is absent in both Slo1 and Slo3 (J. Zhang et al., 2023),
418 further suggesting that zinc regulation differs among Slo family members. Although
419 regions surrounding E191 or E176 may still provide additional insights into zinc regulation
420 and could be of interest for future investigation, E205 stands out because, unlike E169, it
421 is not conserved across the Slo family, making it unique to mSlo3 and potentially a specific
422 determinant of zinc sensitivity in this channel.

423 However, our single amino acid mutations in this site, which contain clustered negative
424 residues, did not significantly change zinc-mediated current reduction compared to the
425 wildtype. This may be due to mutating one single amino acid might not be sufficient to
426 fully elucidate other contributing residues in the predicted mSlo3 zinc binding site. Thus,
427 more extensive mutagenesis studies will be needed to fully understand zinc inhibition in
428 mSlo3.

429 It is worth noting that the incomplete loss of zinc sensitivity in these mutants suggests that
430 additional mechanisms may participate in zinc modulation of Slo3. These may include

431 modulation of nearby charged residues, structural rearrangements influenced by zinc
432 binding, or the presence of multiple zinc binding sites. Comparisons with Slo2.2 (J. Zhang
433 et al., 2023), KCNQ4 (Gao et al., 2017), and voltage-gated calcium channels (Sun et al.,
434 2007) further support the possibility of diverse molecular determinants for zinc inhibition.
435 Our VCF, mutagenesis, and simulation data together indicate that zinc influences voltage
436 sensor movement in mSlo3, which may suggest a distinct inhibitory mechanism that
437 warrants further investigation.

438 **Physiological relevance of zinc inhibition of the mSlo3 channel in mouse sperm**

439 Zinc is thought to be involved in capacitation and the acrosome reaction, suggesting its role
440 in regulating sperm fertilizing ability *in vitro* (Aonuma et al., 1978). This finding is
441 supported by studies indicating that seminal zinc inhibits sperm's ability to undergo the
442 acrosome reaction (Riffo et al., 1992). However, the specific function of intracellular zinc
443 in relation to the capacitation process has not been thoroughly investigated. Previous
444 research indicates that zinc inhibits sperm motility in ejaculation medium as well as
445 acrosome reaction (Henkel et al., 1999; Riffo et al., 1992), leading to the hypothesis that
446 zinc might influence capacitation.

447 Slo3 plays a critical role in sperm fertility, since mice lacking Slo3 are infertile despite
448 their normal sperm morphology (Santi et al., 2010). Furthermore, our previous work
449 showed that VSP-deficient sperm exhibited enhanced Slo3 channel activity, which
450 indirectly increases Ca^{2+} influx and results in abnormal sperm motility (Kawai et al., 2019).
451 Taken together, our findings suggest that intracellular zinc is potentially a key regulator of
452 sperm capacitation, functioning through inhibition of the Slo3 channel. Although these
453 results support a mechanistic link between zinc and Slo3 activity, future studies that
454 combine genetic or pharmacological modulation of Slo3 with comprehensive capacitation
455 analyses will be required to define its physiological impact in more detail. Within this
456 context, this study highlights the potential importance of intracellular zinc in the regulation
457 of sperm capacitation.

458 In addition to that, to date, there are only few reports on the effect of zinc on other sperm
459 ion channels, and none have been reported in mouse sperm. One important study was
460 reported by (Jeschke et al., 2021), in which seminal zinc was found to inhibit prostaglandin-
461 induced activation of CatSper, a sperm-specific Ca^{2+} channel, in human sperm. The
462 complex opposing action of seminal zinc and prostaglandins on CatSper may help
463 preventing premature activation of CatSper in the ejaculate and act as a dilution sensor,
464 although this study does not provide direct evidence for zinc acting directly on CatSper
465 (Jeschke et al., 2021).

466 Taken together, this study provides new insights into the zinc-dependent modulation of
467 sperm ion channels, underscoring the central role of Slo3 and offering a foundation for
468 future exploration of the complex molecular mechanisms governing fertilization.

469 **Materials and Methods**

470 **Ethical approval**

471 All animal experiments were approved by the Animal Care and Use Committee of the
472 Osaka University Graduate School of Medicine and performed in accordance with its
473 guidelines.

474 **Drug and Reagent**

475 Zinc pyrithione was purchased from Fujifilm Wako (Osaka, Japan). TPEN was obtained
476 from Cayman (Ann Arbor, MI, USA). Gramicidin was obtained from Merck (Kenilworth,
477 NJ).

478 **Patch Clamp Recordings from Spermatozoa**

479 Patch clamp recordings from spermatozoa were conducted as previously described (Kawai
480 et al., 2019; Kirichok et al., 2006). Briefly, sperm were harvested from the mouse corpus
481 epididymis using an HS-based solution containing (in mM): 135 NaCl, 5 KCl, 2 $CaCl_2$, 1
482 $MgSO_4$, 20 HEPES, 5 glucose, 10 lactic acid, and 1 sodium pyruvate (pH 7.4). After 10
483 minutes, the supernatant was collected, centrifuged, washed twice with the HS-based
484 solution, resuspended, and placed on untreated glass coverslips.

485 For conventional whole-cell recordings, the intracellular solution contained (in mM): 120
486 KCl, 3 $MgCl_2$, 40 MES, and 0.3 EGTA (pH 6.0), with the osmolality adjusted to
487 approximately 300 mOsm/kg using sucrose. The same HS-based solution was used as the
488 bath solution.

489 For perforated patch recordings, the intracellular solution included (in mM): 120 KCl, 3
490 $MgCl_2$, 40 HEPES, 0.3 EGTA (pH 7.0), and 0.05 mg/ml gramicidin. HS-based solution
491 was used as the extracellular solution. Once pores formed, the access resistance ranged
492 between 50 and 100 MΩ.

493 Recording pipettes were made with borosilicate glass (BF-150-86-10; Sutter Instruments,
494 CA, USA) using a puller (P-97; Sutter Instruments). The recordings were conducted using
495 an Axopatch 200B amplifier (Molecular Devices, CA, USA) and sampled at 5 kHz using
496 a Digidata 1550A system (Molecular Devices) with pCLAMP 10.5 software (Molecular
497 Devices). Low pass filter of 20 Hz was applied to increase S/N ratio.

498 **Zinc imaging from Spermatozoa**

499 Sperm were isolated from the cauda epididymis of mice and transferred to HS medium.
500 The sperm were then loaded with 10 μM FluoZin3-AM (Invitrogen) and 0.05% Pluronic
501 F-127 in HS medium, followed by a 30-minutes incubation at 37ºC. After incubation, the
502 sperm were washed with HS medium and incubated on Cell-Tak (Corning, Bedford, MA)-
503 coated round cover glasses for 10 minutes. The cover glass was mounted on a perfusion
504 chamber for imaging experiments.

505 Fluorescence signals were detected using a filter set (Ex 495/10; DM 515; Em 535/25) with
506 an IX-81 upright microscope (Olympus, Tokyo, Japan) equipped with a C9100 EMCCD
507 camera (Hamamatsu Photonics, Shizuoka, Japan) and Metamorph imaging software
508 (Molecular Devices). Images were captured every 30 seconds. Fluorescence intensity is
509 measured by the signal taken from the whole head and the proximal part of tail in sperm.

510 For capacitation, TYH medium (Toyoda et al., 1971) was used, consisting of: 120 mM
511 NaCl, 4.8 mM KCl, 1.2 mM KH_2PO_4, 5.6 mM glucose, 1.0 mM sodium pyruvate, 1.7 mM

512 $CaCl_2$, 1.2 mM $MgSO_4$, 25 mM $NaHCO_3$, 4.0 g/L ALBMAX I (Thermo Fisher Scientific),
513 and penicillin (50 units/ml)-streptomycin (50 μg/ml).

514 The experiment focused on the head and tail regions of spermatozoa. For analysis, cells in
515 which both the head and tail were visible throughout the entire experiment were selected.

516 **Sperm motility analysis**

517 Sperm velocity was analyzed as previously described (Miyata et al., 2021). Briefly,
518 spermatozoa isolated from the cauda epididymis were suspended in TYH medium. The
519 TYH medium contained: 120 mM NaCl, 4.8 mM KCl, 1.2 mM KH_2PO_4, 5.6 mM glucose,
520 1.0 mM sodium pyruvate, 1.7 mM $CaCl_2$, 1.2 mM $MgSO_4$, 25 mM $NaHCO_3$, 4.0 g/L
521 ALBMAX I (Thermo Fisher Scientific), penicillin (50 units/ml) - streptomycin (50 μg/ml),
522 and 0.6% Phenol Red.

523 Average path velocity (VAP), curvilinear velocity (VCL), straight-line velocity (VSL),
524 straightness (STR), and linearity (LIN) was measured using the CEROS II sperm analysis
525 system (Hamilton Thorne Biosciences, MA, USA) at 10 minutes and 2 hours after
526 incubation. In some experiments, 20 μM TPEN was directly added to the TYH medium.

527 **Molecular Biology**

528 All Slo3 mutants were constructed from WT *mus musculus* Slo3 (mSlo3) in PSD64TF.
529 Single amino acid mutations were introduced using PrimeSTAR Mutagenesis Basal Kit
530 (Takara Bio Inc.). Chimeras were generated using In-Fusion HD Cloning Kit (Takara Bio
531 Inc.). The introduced mutations and generated chimeras were confirmed by DNA
532 sequencing. The mMESSAGE SP6 RNA transcription kit (Thermo Fisher Scientific) was
533 used to transcribe WT, mutants, and chimeras of mSlo3 cRNAs from plasmid cDNA
534 linearized by Xba1 restriction enzyme (Takara Bio Inc.).

535 **Preparation of *Xenopus* laevis oocytes**

536 As an anesthetic agent, 0.15% tricaine (Sigma-Aldrich / Tokyo Chemical Industry) was
537 used for *Xenopus* laevis before surgical operation for isolation of oocytes. Follicular

538 membranes were removed from isolated oocytes by collagenase treatment (2 mg ml−1;
539 type 1; Sigma-Aldrich or Collagenase-P from Roche) for 3 hr. Oocytes were then rinsed
540 and stored in ND96 solution (96 mM NaCl, 2 mM KCl, 1.8 mM $CaCl_2$, 1 mM $MgCl_2$, and
541 5 mM 2-[4-(2-Hydroxyethyl)-1-piperazinyl]ethanesulfonic acid (HEPES), pH 7.5, with
542 NaOH) supplemented with 0.1 mg/mL gentamycin (FUJIFILM Wako Pure Chemical
543 Corporation or Nacalai Tesque, Inc.) and 5 mM sodium pyruvate. The incubation
544 temperature was 18 °C.

545 **Expression of mSlo3 channel**

546 *Xenopus* oocytes injected with 15 ng of WT mSlo3 cRNA and incubated for 2 days at 18°C.
547 For mSlo3 mutants, oocytes were injected with 50 ng–60 ng of cRNA and incubated for
548 1–3 days, depending on the desired expression level for patch-clamp and voltage-clamp
549 fluorometry (VCF) experiments. cRNA for mLrrc52 was also injected for data shown in
550 Fig. 3, Fig. 3—figure supplement 1, Fig. 6, and Fig. 6—figure supplement 1F-H.

551 **Oocyte patch-clamp recording of mSlo3**

552 Patch-clamp recordings of *Xenopus* oocytes were performed using an Axopatch-200B
553 amplifier (Molecular Devices) connected through an AD/DA converter (Digidata 1440A:
554 Molecular Devices) and operated with pClamp software. Current traces were filtered at 5
555 kHz and sampled at 100 kHz. Vitelline membrane was manually removed using forceps
556 after incubation for 1 to 5-minute in a hypertonic solution containing 192 mM NMDG, 4
557 mM KCl, 3.6 mM $CaCl_2$, 2 mM $MgCl_2$, and 10 mM HEPES, pH 7.4, with HCl. Leak
558 currents were subtracted by using a P/-8 protocol for step pulses recordings only. Patch
559 pipettes, with resistance ranging from 1 to 3 MΩ were pulled from borosilicate glass
560 (Drummond Scientific Company). The pipette solution contains 0.5 mM potassium
561 gluconate, 0.5 mM KCl, 1.1 mM KOH, 10 mM HEPES, 159 mM sodium gluconate, and 2
562 mM $MgCl_2$, pH 7.1, adjusted with methanesulfonic acid.

563 Patches were perfused with: (1) bath solution containing 184 mM potassium gluconate, 10
564 mM KOH and 10 mM HEPES in pH 6.0, 7.5, and 8.0; (2) zinc-containing bath solution at
565 pH 7.5 and pH 8.0, with zinc concentrations of 0.1, 1, 10, 100, and 1000 μM. (3) bath

566 solution containing 5 mM EGTA in pH 8.0. All pH values were adjusted using
567 methanesulfonic acid. Slo3 macroscopic currents were evoked by an alkaline pH and by a
568 depolarizing ramp pulse (from -100 mV to +100 mV with the holding potential of either -
569 60 mV or 0 mV) or step pulses (from -100 mV to +180 mV with the holding potential at -
570 60 mV). All bath solutions were perfused using a high-speed perfusion system ALA-VM8
571 OCTAFLOW (ALA Scientific Instruments Inc.)

572 **Voltage-clamp fluorometry (VCF) recording of mSlo3**

573 In mSlo3 VCF construct, the target labeling site (in S3-S4 linker) was substituted with
574 cysteine residue. Two native, extracellular cysteines were mutated to avoid non-specific
575 labeling (mSLo3 C19S/C131S). Oocytes for VCF recordings were labeled with
576 Tetramethylrhodamine-5-maleimide (TMRM) (Invitrogen). In prior to VCF recordings,
577 oocytes were incubated in a labeling solutions (120 mM K-methanesulfonate (MES), 2
578 mM $CaCl_2$, and 10 mM HEPES pH 7.4) containing 10 µM TMRM (Savalli et al., 2006) on
579 ice for 1 hour. Labeled oocytes were then rinsed in TMRM-free ND96 solution four times
580 and kept in the dark until and throughout the recording.

581 Oocytes were placed in a recording chamber with the animal pole facing upward and held
582 at -60 mV. For screening experiments, step pulses ranging from -80 mV to +160 mV were
583 applied, while pulses from -160 mV to +160 mV were used for direct zinc injection
584 experiments. For the VCF recording in the absence and presence of zinc, voltage steps were
585 first applied to record the initial response. Subsequently, a puff of 10 mM zinc solution
586 was manually injected into the same oocyte using a glass needle and positive pressure.
587 Sixty seconds post-injection, a second set of step pulses was applied to record the response
588 under zinc application. In VCF recording, borosilicate glass capillaries (Harvard
589 Apparatus) were used with a resistance of 0.2–0.4 MΩ when filled with 3 M KOAc and 10
590 mM KCl. Bath solution contained 96 mM NaCl, 2 mM KCl, 1.8 mM $CaCl_2$, 1 mM $MgCl_2$,
591 and 5 mM HEPES, pH 7.4-7.5, with NaOH was used for recordings.

592 Fluorometric recordings were performed with an upright fluorescence microscope
593 (Olympus BX50WI) equipped with a water immersion objective lens (Olympus
594 XLUMPLAN FL 20x/1.00) to collect the emission light from the voltage-clamped oocytes.

595 The light from LED source (MCWHL8 Thorlabs) was applied through a band-pass
596 excitation filter (531 nm/40 nm BrightLine: Semrock). Emitted light was passed through
597 band pass emission filter of 593nm/40nm (BrightLine, Semrock). The emission signals
598 were detected by a photomultiplier (H10722-20; Hamamatsu Photonics). The detected
599 emission intensities were acquired by a Digidata 1440A (Axon Instruments) and Clampex
600 10.3 software (Molecular Devices) at 25 kHz for VCF mutants screening and 50 kHz for
601 VCF recording in the absence and presence of zinc. To improve the signal-to-noise ratio,
602 VCF recording was repeated 3 times. Averaged data were used for data presentation and
603 analysis.

604

605 **Three-dimensional structural modeling of mouse Slo3 and prediction of zinc binding**
606 **site**

607 The amino acid sequence of mouse Slo3 (mSlo3) (O54982-1) was obtained from the
608 UniProt database (Fig. 4) and was retrieved from NCBI NP_032458.3 (Fig. 5). The
609 sequence (only the transmembrane region from residue M1 to G330, or the full-length
610 protein) was input to the AlphaFold3 (Abramson et al., 2024) structural modelling web
611 platform to generate an initial structure with (Fig. 4A) or without (Fig. 5A) 50 zinc ions.
612 All the structural data presented in this study were generated using PyMOL molecular
613 graphics system ver. 2.5.0 (Schrodinger LLC).

614 **Flooding simulations**

615 The full-length mSlo3 from the AlphaFold3 webserver was trimmed to remove long
616 disordered regions (residue 1-18, 616-698 and 1050-1121), resulting in 12 separate chains.
617 The mSlo3 complex was embedded into the POPC bilayer and solvated in 0.15 M NaCl
618 and 0.15 $ZnCl_2$ using CHARMM-GUI Membrane Builder (Wu et al., 2014). The
619 production run simulations were simulated with a 2 fs timestep using the CHARMM36m
620 forcefield (Huang et al., 2016) in GROMACS 2023.3 (Abraham et al., 2023). The system
621 was then energy minimized and equilibrated using the standard six steps CHARMM-GUI
622 equilibration protocol. This includes the following set-up: The protein backbone was

restrained at the force constant of 4000, 2000, 1000, 500, 200 and 50 $kJmol^{-1}nm^{-2}$, the protein side chains were restrained with the force constant of 2000, 1000, 500, 200, 50, and 0 $kJmol^{-1}nm^{-2}$, the lipids non-H atoms were restrained at the force constant of 1000, 400, 400, 200, 40 and 0 $kJmol^{-1}nm^{-2}$ and the dihedral restraint was set at the force constant of 1000, 400, 200, 200, 100 and 0 $kJmol^{-1}rad^{-2}$. The simulations were equilibrated with a 1 fs timestep for 125 ps for the first three steps, and then to a 2 fs timestep for 500 ps the next two, and 5 ns for the final step. The first two steps were conducted with the NVT ensemble, whereas the last four were conducted with the NPT ensemble. All equilibration runs were conducted at 310 K using Berendsen thermostat (Berendsen et al., 1984). In all NPT ensemble equilibration, the semi-isotropic pressure was maintained at 1 bar using Berendsen barostat. The production runs were conducted for 200 ns under 310 K using the v-rescale thermostat (Bussi et al., 2007). The semi-isotropic pressure of all systems was maintained at 1 bar using a C-rescale barostat (Bernetti & Bussi, 2020). All simulations were carried out in triplicates, where velocity was randomly generated at the beginning of every simulation. All simulation frames were saved every 0.1 ns.

Zn stability

Based on the flooding simulations, the binding pose for Zn^{2+} is adjusted so that the ion is 3-4 Å away from E169. This results in the system with 4 Zn^{2+} per system, one per subunit. The system was then energy minimized using the steepest descent algorithm and equilibrated with the Cα restraint at 1000 kJ $kJmol^{-1}nm^{-2}$ for 10 ns. The production run was conducted for 200 ns, with the same barostat and thermostat setting as the flooding simulation.

Data Analysis

Inside-out patch-clamp data were analyzed using Clampfit 11.3 software (Molecular Devices), Igor Pro 6.22A (Wavemetrics), and GraphPad Prism 10. Analysis of current-voltage (I-V) were obtained from the maximum current amplitude at steady-state. Normalization for figure 2H was performed by dividing the absolute current of mSlo3 at pH 8.0 of each voltage by the absolute current at the pre-determined highest voltage that

651 still produced a stable mSlo3 current (i.e., good patch, good clamp). In this analysis, +140
652 mV was chosen as the highest voltage for normalization, since in few cells the patch was
653 lost at +160mV and +180mV. Similar to the control condition, the absolute current of
654 mSlo3 in the presence of 100 µM zinc was normalized to the absolute current of the control
655 at +140 mV. I-V relationship was fitted with Boltzmann equation:

656 $$I(V) = \frac{G}{1+\exp(\frac{V50-V}{s})} \times (V - V_{rev}) \quad (1)$$

657 where G is a scaling factor (maximum conductance or current), V_{50} is the midpoint, and s
658 is the slope value.

659 And then the I-V relationship in the presence of 100 µM of $ZnCl_2$ was fitted with Woodhull
660 equation (Woodhull, 1973) to express the current as a function of voltage, incorporating
661 both the voltage-dependent gating of the channel and the voltage-dependent blocking of
662 the channel:

663 $$I(V) = \frac{G}{1+\exp(\frac{V50-V}{s})} \times (V - V_{rev}) \times \frac{1}{1+\exp(\frac{Vblock-V}{Slopeblock})} \quad (2)$$

664 $$Slope_{block} = \frac{RT}{-\delta zF} \quad (3)$$

665 where V_{block} is the voltage at which blocking is half-maximal, $Slope_{block}$ is the slope factor
666 for the voltage dependence of the blocking effect, and δ is the fraction of the membrane
667 potential that the blocking ion experiences.

668 V_{rev} is the reversal potential and was calculated with following equation as described in
669 (Schreiber et al., 1998) using Goldman-Hodgkin-Katz equation:

670 $$E_{rev} = \frac{RT}{F} \ln \frac{[K^+]_{out} + P\,[Na^+]_{out}}{[K^+]_{in} + P\,[Na^+]_{in}} \quad (4)$$

671 where P is the Na^+ to K^+ permeability ratio (Schreiber et al., 1998).

672 Conductance-voltage (G-V) relationship of Slo3 were obtained from conductance
673 calculation using the following equation:

674 $$G(V) = \frac{I}{V - V_{rev}} \quad (5)$$

675 V_{rev} was calculated using equation (4) and fitted to Boltzmann equation in (1), adjusted for
676 G-V.

677 IC_{50} (half maximal inhibitory concentration) was calculated using equation while
678 constraining the Hill Slope to a constant value of -1.0:

679 $$Y = I_{min} + \frac{I_{max} - I_{min}}{1 + \frac{IC_{50}}{X}} \quad (6)$$

680 where I_{max} is the maximal current when inhibition is minimal, I_{min} is the minimal current
681 inhibition is maximal, and X is the inhibitor concentration.

682 Arithmetic operations were performed by Clampfit to compensate bleaching from the
683 fluorescence traces:

684 $$[\text{Compensated trace}] = [\text{Recorded Ftrace}] \times (1 - (R \times [\text{time}])) \quad (7)$$

685 where [time] is the value of the point given by Clampfit.

686 All the compensated traces were then normalized by setting each baseline level (F signal
687 at −60 mV, the holding potential) to be 1, to calculate the % F change:

688 $$(\Delta F/F;\ \Delta F = F_{+160mV} - F_{baseline};\ F = F_{baseline}) \quad (8)$$

689 Conductance-voltage (G-V) relationship for VCF data were obtained from conductance
690 calculation using equation (5). Fluorescence-voltage (F-V) relationship were obtained from
691 the normalized ΔF/F and fitted with the equation (1).

692

693 **Statistical analysis**

694 Statistical analysis was performed by either one-way ANOVA, unpaired t-test or paired t-
695 test. Following one-way ANOVA, Dunnett's post-hoc test was applied. The data were
696 expressed as mean± s.e.m. with n indicating the number of samples. Values of p were stated

in each bar graph. All the statistical analysis and the bar graphs were performed and generated with GraphPad Prism 10.

Acknowledgments

The authors thank Prof. Fredrik Elinder (Linköping University, Sweden) for discussion and the guidance on analysis and experiments, Ms. Hikari Ginama and Ms. Megumi Kobayashi for technical support and Dr. Natsuki Mizutani for discussion and guidance of experiment. This work was supported by fundings provided by Grants-in-Aid from MEXT KAKENHI Grant Number JP20H05507 (T.K), JP20H05791 (Y.O), JP22K15074 (R.T.A), JSPS KAKENHI Grant Number JP17K15558, JP23K06334 (T.K), 19H03401, 22H02804 (Y.O), and JST FOREST Program Grant Number JPMJFR225Z (T.K). The research is supported by JSPS Postdoctoral Fellowship for Research in Japan (R.T.A) and Lee Kuan Yew Postdoctoral Fellowship from Nanyang Technological University, Singapore (T.P). Additionally, financial support was received from the Takeda Science Foundation and Mochida Memorial Foundation for Medical and Pharmaceutical Research, all of which contributed to T.K.‘s research.

References

Abraham, M., Alekseenko, A., Bergh, C., Blau, C., Briand, E., Doijade, M., Fleischmann, S., Gapsys, V., Garg, G., Gorelov, S., Gouaillardet, G., Gray, A., Irrgang, M. E., Jalalypour, F., Jordan, J., Junghans, C., Kanduri, P., Keller, S., Kutzner, C., … Lindahl, E. (2023). *GROMACS 2023.3 Source code*. Zenodo. https://doi.org/10.5281/zenodo.10017686

Abramson, J., Adler, J., Dunger, J., Evans, R., Green, T., Pritzel, A., Ronneberger, O., Willmore, L., Ballard, A. J., Bambrick, J., Bodenstein, S. W., Evans, D. A., Hung, C. C., O’Neill, M., Reiman, D., Tunyasuvunakool, K., Wu, Z., Žemgulytė, A., Arvaniti, E., … Jumper, J. M. (2024). Accurate structure prediction of biomolecular interactions with AlphaFold 3. *Nature*, *630*(8016), 493–500. https://doi.org/10.1038/s41586-024-07487-w

Aonuma, S., Okabe, M., & Kawaguchi, M. (1978). The effect of zinc ions on fertilization

of mouse ova in vitro. *Journal of Reproduction and Fertility*, *53*(1), 179–183. https://doi.org/10.1530/jrf.0.0530179

Arnoult, C., Kazam, I. G., Visconti, P. E., Kopf, G. S., Villaz, M., & Florman, H. M. (1999). Control of the low voltage-activated calcium channel of mouse sperm by egg ZP3 and by membrane hyperpolarization during capacitation. *Proceedings of the National Academy of Sciences of the United States of America*, *96*(12), 6757–6762. https://doi.org/10.1073/pnas.96.12.6757

Austin, C. R. (1951). Observations on the penetration of the sperm in the mammalian egg. *Australian Journal of Scientific Research. Ser. B: Biological Sciences*, *4*(4), 581–596. https://doi.org/10.1071/bi9510581

Berendsen, H. J. C., Postma, J. P. M., Van Gunsteren, W. F., Dinola, A., & Haak, J. R. (1984). Molecular dynamics with coupling to an external bath. *The Journal of Chemical Physics*, *81*(8), 3684–3690. https://doi.org/10.1063/1.448118

Bernetti, M., & Bussi, G. (2020). Pressure control using stochastic cell rescaling. *Journal of Chemical Physics*, *153*(11). https://doi.org/10.1063/5.0020514

Breitbart, H. (2002). *Intracellular calcium regulation in sperm capacitation and acrosomal reaction*. *187*, 139–144.

Budelli, G., Sun, Q., Ferreira, J., Butler, A., Santi, C. M., & Salkoff, L. (2016). SLO2 Channels are inhibited by all divalent cations that activate SLO1 K- channels. *Journal of Biological Chemistry*, *291*(14), 7347–7356. https://doi.org/10.1074/jbc.M115.709436

Bussi, G., Donadio, D., & Parrinello, M. (2007). Canonical sampling through velocity rescaling. *Journal of Chemical Physics*, *126*(1). https://doi.org/10.1063/1.2408420

Chang, M. C. (1951). Fertilizing Capacity of Spermatozoa deposited into the Fallopian Tubes. *Nature*, *168*(4277), 697–698. https://doi.org/10.1038/168697b0

Chia, S., Ong, C., Chua, L., & Ho, L. (2000). Comparison of Zinc Concentrations in

751 Blood and Seminal. *Journal of Andrology*, *21*(1), 53–58.

752 Elgazar, V., Razanov, V., Stoltenberg, M., Hershfinkel, M., Huleihel, M., Nitzan, Y. B.,
753 Lunenfeld, E., Sekler, I., & Silverman, W. F. (2005). Zinc-regulating proteins, ZnT-
754 1, and metallothionein I/II are present in different cell populations in the mouse
755 testis. *Journal of Histochemistry and Cytochemistry*, *53*(7), 905–912.
756 https://doi.org/10.1369/jhc.4A6482.2005

757 Fallah, A., Mohammad-Hasani, A., & Colaga, A. H. (2018). Zinc is an essential element
758 for male fertility : a review of Zn roles in men ' s. *J Reprod Infertil*, *19*(2), 69–81.

759 Fayyazuddin, A., Villarroel, A., Le Goff, A., Lerma, J., & Neyton, J. (2000). Four
760 residues of the extracellular N-terminal domain of the NR2A subunit control high-
761 affinity Zn2+ binding to NMDA receptors. *Neuron*, *25*(3), 683–694.
762 https://doi.org/10.1016/S0896-6273(00)81070-3

763 Gao, H., Boillat, A., Huang, D., Liang, C., Peers, C., & Gamper, N. (2017). Intracellular
764 zinc activates KCNQ channels by reducing their dependence on phosphatidylinositol
765 4,5-bisphosphate. *Proceedings of the National Academy of Sciences of the United*
766 *States of America*, *114*(31), E6410–E6419. https://doi.org/10.1073/pnas.1620598114

767 Grahn, E., Kaufmann, S. V., Askarova, M., Ninov, M., Welp, L. M., Berger, T. K.,
768 Urlaub, H., & Kaupp, U. B. (2023). Control of intracellular pH and bicarbonate by
769 CO2 diffusion into human sperm. *Nature Communications*, *14*(1).
770 https://doi.org/10.1038/s41467-023-40855-0

771 Henkel, R., Bittner, J. örg, Weber, R., Hüther, F., & Miska, W. (1999). Relevance of zinc
772 in human sperm flagella and its relation to motility. *Fertility and Sterility*, *71*(6),
773 1138–1143. https://doi.org/10.1016/S0015-0282(99)00141-7

774 Henkel, R., Maass, G., Schuppe, H. C., Jung, A., Schubert, J., & Schill, W. B. (2005).
775 Molecular aspects of declining sperm motility in older men. *Fertility and Sterility*,
776 *84*(5), 1430–1437. https://doi.org/10.1016/j.fertnstert.2005.05.020

Hou, S., Vigeland, L. E., Zhang, G., Xu, R., Li, M., Heinemann, S. H., & Hoshi, T. (2010). Zn2+ activates large conductance Ca2+-activated K+ channel via an intracellular domain. *Journal of Biological Chemistry*, *285*(9), 6434–6442. https://doi.org/10.1074/jbc.M109.069211

Hu, H., Bandell, M., Petrus, M. J., Zhu, M. X., & Patapoutian, A. (2009). Zinc activates damage-sensing TRPA1 ion channels. *Nature Chemical Biology*, *5*(3), 183–190. https://doi.org/10.1038/nchembio.146

Huang, J., Rauscher, S., Nawrocki, G., Ran, T., Feig, M., De Groot, B. L., Grubmüller, H., & MacKerell, A. D. (2016). CHARMM36m: An improved force field for folded and intrinsically disordered proteins. *Nature Methods*, *14*(1), 71–73. https://doi.org/10.1038/nmeth.4067

Jeschke, J. K., Biagioni, C., Schierling, T., Wagner, I. V., Börgel, F., Schepmann, D., Schüring, A., Kulle, A. E., Holterhus, P. M., Wolff, M. Von, Wünsch, B., Nordhoff, V., Strünker, T., & Brenker, C. (2021). *The Action of Reproductive Fluids and Contained Steroids , Prostaglandins , and Zn 2 + on CatSper Ca 2 + Channels in Human Sperm*. *9*(July), 1–16. https://doi.org/10.3389/fcell.2021.699554

Kambe, T., Yamaguchi-Iwai, Y., Sasaki, R., & Nagao, M. (2004). Overview of mammalian zinc transporters. *Cellular and Molecular Life Sciences*, *61*(1), 49–68. https://doi.org/10.1007/s00018-003-3148-y

Kawai, T., Miyata, H., Nakanishi, H., Sakata, S., Morioka, S., Sasaki, J., Watanabe, M., Sakimura, K., Fujimoto, T., Sasaki, T., Ikawa, M., & Okamura, Y. (2019). Polarized PtdIns(4,5)P2 distribution mediated by a voltage-sensing phosphatase (VSP) regulates sperm motility. *Proceedings of the National Academy of Sciences of the United States of America*, *116*(51), 26020–26028. https://doi.org/10.1073/pnas.1916867116

Kerns, K., Zigo, M., Drobnis, E. Z., Sutovsky, M., & Sutovsky, P. (2018). Zinc ion flux during mammalian sperm capacitation. *Nature Communications*, *9*(1).

804 https://doi.org/10.1038/s41467-018-04523-y

805 Kirichok, Y., Navarro, B., & Clapham, D. E. (2006). Whole-cell patch-clamp
806 measurements of spermatozoa reveal an alkaline-activated Ca2+ channel. *Nature*,
807 *439*(7077), 737–740. https://doi.org/10.1038/nature04417

808 Leonetti, M. D., Yuan, P., Hsiung, Y., & MacKinnon, R. (2012). Functional and
809 structural analysis of the human SLO3 pH- and voltage-gated K+ channel.
810 *Proceedings of the National Academy of Sciences of the United States of America*,
811 *109*(47), 19274–19279. https://doi.org/10.1073/pnas.1215078109

812 Lishko, P. V., Botchkina, I. L., Fedorenko, A., & Kirichok, Y. (2010). Acid Extrusion
813 from Human Spermatozoa Is Mediated by Flagellar Voltage-Gated Proton Channel.
814 *Cell*, *140*(3), 327–337. https://doi.org/10.1016/j.cell.2009.12.053

815 Lyon, M., Li, P., Ferreira, J. J., Lazarenko, R. M., Kharade, S. V, Kramer, M.,
816 McClenahan, S. J., Days, E., Bauer, J. A., Spitznagel, B. D., Weaver, C. D., Alvarez,
817 A. B., Molina, L. C. P., Lybaert, P., Khambekar, S., Liu, A., Lindsley, C. W.,
818 Denton, J., & Santi, C. M. (2023). A selective inhibitor of the sperm-specific
819 potassium channel SLO3 impairs human sperm function. *Proceedings of the*
820 *National Academy of Sciences*, *120*(4), e2212338120.
821 https://doi.org/10.1073/pnas.2212338120

822 Madshus, I. H. (1988). Regulation of intracellular pH in eukaryotic cells. *The*
823 *Biochemical Journal*, *250*(1), 1–8. https://doi.org/10.1042/bj2500001

824 Maret, W. (2013). Zinc biochemistry: From a single zinc enzyme to a key element of life.
825 *Advances in Nutrition*, *4*(1), 82–91. https://doi.org/10.3945/an.112.003038

826 Miyata, H., Oura, S., Morohoshi, A., Shimada, K., Mashiko, D., Oyama, Y., Kaneda, Y.,
827 Matsumura, T., Abbasi, F., & Ikawa, M. (2021). SPATA33 localizes calcineurin to
828 the mitochondria and regulates sperm motility in mice. *Proceedings of the National*
829 *Academy of Sciences of the United States of America*, *118*(35), 1–9.
830 https://doi.org/10.1073/pnas.2106673118

Navarro, B., Kirichok, Y., & Clapham, D. E. (2007). KSper, a pH-sensitive K+ current that controls sperm membrane potential. *Proceedings of the National Academy of Sciences of the United States of America*, *104*(18), 7688–7692. https://doi.org/10.1073/pnas.0702018104

Paoletti, P., Ascher, P., & Neyton, J. (1997). High-affinity zinc inhibition of NMDA NR1-NR2A receptors. *Journal of Neuroscience*, *17*(15), 5711–5725. https://doi.org/10.1523/jneurosci.17-15-05711.1997

Publicover, S., Harper, C. V, & Barratt, C. (2007). *[Ca 2 +] i signalling in sperm — making the most of what you ' ve got*. *9*(3), 235–242.

Riffo, M., Leiva, S., & Astudillo, J. (1992). Effect of zinc on human sperm motility and the acrosome reaction. *International Journal of Andrology*, *15*(3), 229–237. https://doi.org/10.1111/j.1365-2605.1992.tb01343.x

Santi, C. M., Martínez-López, P., de la Vega-Beltrán, J. L., Butler, A., Alisio, A., Darszon, A., & Salkoff, L. (2010). The SLO3 sperm-specific potassium channel plays a vital role in male fertility. *FEBS Letters*, *584*(5), 1041–1046. https://doi.org/10.1016/j.febslet.2010.02.005

Savalli, N., Kondratiev, A., Toro, L., & Olcese, R. (2006). Voltage-dependent conformational changes in human Ca2+- and voltage-activated K+ channel, revealed by voltage-clamp fluorometry. *Proceedings of the National Academy of Sciences of the United States of America*, *103*(33), 12619–12624. https://doi.org/10.1073/pnas.0601176103

Schreiber, M., Wei, A., Yuan, A., Gaut, J., Saito, M., & Salkoff, L. (1998). Slo3, a novel pH-sensitive K+ channel from mammalian spermatocytes. *Journal of Biological Chemistry*, *273*(6), 3509–3516. https://doi.org/10.1074/jbc.273.6.3509

Sørensen, M. B., Stoltenberg, M., Danscher, G., & Ernst, E. (1999). Chelation of intracellular zinc ions affects human sperm cell motility. *Molecular Human Reproduction*, *5*(4), 338–341. https://doi.org/10.1093/molehr/5.4.338

858 Sun, H. S., Hui, K., Lee, D. W. K., & Feng, Z. P. (2007). Zn2+ sensitivity of high- and
859 low-voltage activated calcium channels. *Biophysical Journal*, *93*(4), 1175–1183.
860 https://doi.org/10.1529/biophysj.106.103333

861 Toyoda, T., Yokoyama, M., & Hosi, T. (1971). In vitro fertilization of eggs by fresh
862 epididymal sperm. *Japanese Journal of Animal Reproduction*, *16*(4).
863 https://doi.org/10.1262/jrd1955.16.147

864 Trombley, P. Q., Blakemore, L. J., & Hill, B. J. (2011). Zinc modulation of glycine
865 receptors. *Neuroscience*, *186*, 32–38.
866 https://doi.org/10.1016/j.neuroscience.2011.04.021

867 Vallee, B. L., & Falchuk, K. H. (1993). The biochemical basis of zinc physiology. In
868 *Physiological Reviews* (Vol. 73, Issue 1).
869 https://doi.org/10.1152/physrev.1993.73.1.79

870 Vredenburgh-Wilberg, W. L., & Parrish, J. J. (1995). Intracellular pH of bovine sperm
871 increases during capacitation. *Molecular Reproduction and Development*, *40*(4),
872 490–502. https://doi.org/10.1002/mrd.1080400413

873 Woodhull, A. M. (1973). Ionic Blockage of Sodium Channels in Nerve. *Journal of*
874 *General Physiology*, *61*, 687–708.

875 Wu, E. L., Cheng, X., Jo, S., Rui, H., Song, K. C., Dávila-Contreras, E. M., Qi, Y., Lee,
876 J., Monje-Galvan, V., Venable, R. M., Klauda, J. B., & Im, W. (2014). CHARMM-
877 GUI membrane builder toward realistic biological membrane simulations. *Journal of*
878 *Computational Chemistry*, *35*(27), 1997–2004. https://doi.org/10.1002/jcc.23702

879 Yamaguchi, S., Miura, C., Kikuchi, K., Celino, F. T., Agusa, T., Tanabe, S., & Miura, T.
880 (2009). Zinc is an essential trace element for spermatogenesis. *Proceedings of the*
881 *National Academy of Sciences of the United States of America*, *106*(26), 10859–
882 10864. https://doi.org/10.1073/pnas.0900602106

883 Yang, C., Zeng, X. H., Zhou, Y., Xia, X. M., & Lingle, C. J. (2011). LRRC52 (leucine-

884 rich-repeat-containing protein 52), a testis-specific auxiliary subunit of the
885 alkalization-activated Slo3 channel. *Proceedings of the National Academy of*
886 *Sciences of the United States of America*, *108*(48), 19419–19424.
887 https://doi.org/10.1073/pnas.1111104108

888 Zeng, X. H., Yang, C., Kim, S. T., Lingle, C. J., & Xia, X. M. (2011). Deletion of the
889 Slo3 gene abolishes alkalizationactivated K+ current in mouse spermatozoa.
890 *Proceedings of the National Academy of Sciences of the United States of America*,
891 *108*(14), 5879–5884. https://doi.org/10.1073/pnas.1100240108

892 Zeng, X. H., Yang, C., Xia, X. M., Liua, M., & Lingle, C. J. (2015). SLO3 auxiliary
893 subunit LRRC52 controls gating of sperm KSPER currents and is critical for normal
894 fertility. *Proceedings of the National Academy of Sciences of the United States of*
895 *America*, *112*(8), 2599–2604. https://doi.org/10.1073/pnas.1423869112

896 Zeng, Y., Clark, E. N., & Florman, H. M. (1995). Sperm membrane potential:
897 Hyperpolarization during capacitation regulates zona pellucida-dependent acrosomal
898 secretion. In *Developmental Biology* (Vol. 171, Issue 2, pp. 554–563).
899 https://doi.org/10.1006/dbio.1995.1304

900 Zeng, Y., Oberdorf, J. A., & Florman, H. M. (1996). pH regulation in mouse sperm:
901 Identification of Na+-, Cl--, and HCO-3-dependent and arylaminobenzoate-
902 dependent regulatory mechanisms and characterization of their roles in sperm
903 capacitation. *Developmental Biology*, *173*(2), 510–520.
904 https://doi.org/10.1006/dbio.1996.0044

905 Zhang, J., Liu, S., Fan, J., Yan, R., Huang, B., Zhou, F., Yuan, T., Gong, J., Huang, Z., &
906 Jiang, D. (2023). Structural basis of human Slo2.2 channel gating and modulation.
907 *Cell Reports*, *42*(8), 112858. https://doi.org/10.1016/j.celrep.2023.112858

908 Zhang, X., Zeng, X., & Lingle, C. J. (2006). Slo3 K+ channels: Voltage and pH
909 dependence of macroscopic currents. *Journal of General Physiology*, *128*(3), 317–
910 336. https://doi.org/10.1085/jgp.200609552

Zhao, R., Kennedy, K., De Blas, G. A., Orta, G., Pavarotti, M. A., Arias, R. J., de la Vega-Beltrán, J. L., Li, Q., Dai, H., Perozo, E., Mayorga, L. S., Darszon, A., & Goldstein, S. A. N. (2018). Role of human Hv1 channels in sperm capacitation and white blood cell respiratory burst established by a designed peptide inhibitor. *Proceedings of the National Academy of Sciences of the United States of America*, *115*(50), E11847–E11856. https://doi.org/10.1073/pnas.1816189115

Zheng, F., Erreger, K., Low, C. M., Banke, T., Lee, C. J., Conn, P. J., & Traynelis, S. F. (2001). Allosteric interaction between the amino terminal domain and the ligand binding domain of NR2A. *Nature Neuroscience*, *4*(9), 894–901. https://doi.org/10.1038/nn0901-894

Zhu, X., Yu, C., Wu, W., Shi, L., Jiang, C., Wang, L., Ding, Z., & Liu, Y. (2022). Zinc transporter ZIP12 maintains zinc homeostasis and protects spermatogonia from oxidative stress during spermatogenesis. *Reproductive Biology and Endocrinology*, *20*(1), 1–15. https://doi.org/10.1186/s12958-022-00893-7

Figures

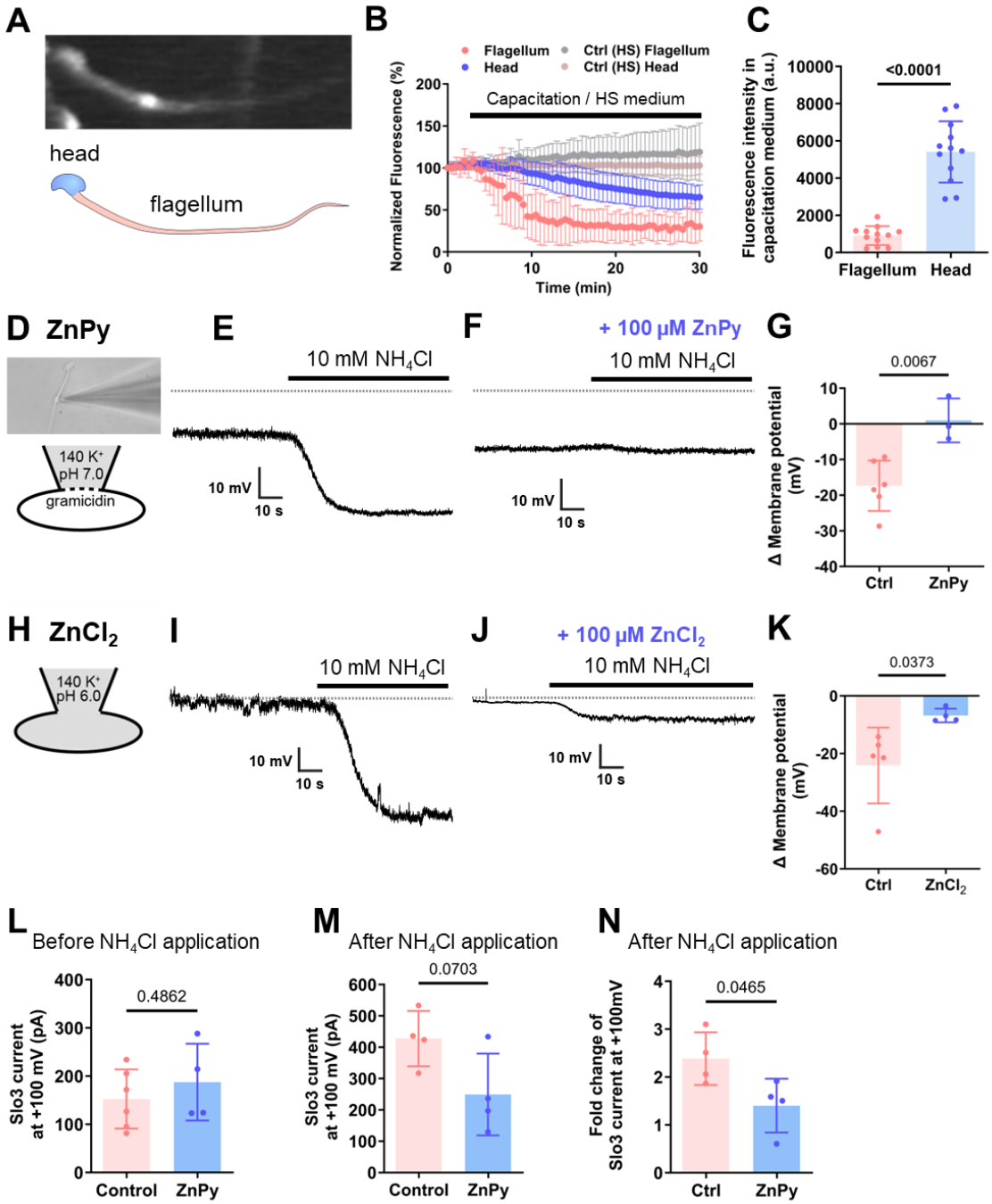

Figure 1. Intracellular zinc is exported from sperm during capacitation and inhibits the alkalinization-induced hyperpolarization in sperm. (**A-C**) Intracellular zinc is exported from sperm during capacitation. (**A**) Representative image of FluoZin3-AM fluorescence observed in spermatozoa (head and flagellum, as indicated). (**B**) Time course of normalized FluoZin3-AM

fluorescence response upon the application of capacitation medium. Both head and flagellum showed a decreased fluorescence response, indicating that intracellular zinc was exported from sperm in response to the application of capacitation medium. (**C**) Comparison of the fluorescence intensity from flagellum (908.6 ± 508.2; n=12) and head (5409 ± 1648; n=12) after capacitation. Unpaired t-test, $p<0.0001$. All error bars are ± SD centered on the mean. (**D-H**) Intracellular zinc inhibits the alkalinization-induced hyperpolarization in sperm. (**D-G**) Membrane potential (Vm) recording by perforated patch-clamp were performed in mouse spermatozoa as depicted in (**D**). (**E**) Representative trace of Vm recording for control group. The application of NH_4Cl increased the intracellular pH (pHi) which then hyperpolarized the membrane, the process called alkalinization-induced hyperpolarization. Application of NH_4Cl alone hyperpolarized the membrane by -17.37 ± 7.09 mV (n=6). (**F**) Representative trace of Vm recording in the presence of zinc ionophore (zinc pyrithione, ZnPy). When 100 µM ZnPy was applied on the top of NH_4Cl application, no hyperpolarization was observed (ΔVm = 0.99 ± 6.17 mV; n=3). All the dotted lines indicated 0 mV level. (**G**) Comparison of ΔVm recording between control (n=6) and in the presence of 100 µM ZnPy (n=3), p=0.0067, unpaired t-test. (**H-K**) Vm recording by whole-cell patch-clamp configuration in mouse spermatozoa as depicted in (**H**). (**I**) Representative trace of Vm recording for control group. The application of NH_4Cl increased the [pHi] which then hyperpolarized the membrane (ΔVm= -24.12 ± 13.16 mV; n=5). (**J**) Representative trace of Vm recording in the presence of 100 µM $ZnCl_2$. When zinc was applied to the intracellular part of spermatozoa on top of NH_4Cl application, alkalinization-induced hyperpolarization was inhibited (ΔVm= -6.80 ± 2.35 mV; n=4). All the dotted line indicated 0 mV level. (**K**) Comparison of ΔVm recording between control (n=5) and in the presence of 100 µM $ZnCl_2$ (n=4), p=0.0373, unpaired t-test. (**L-N**) Slo3 current recording using perforated patch-clamp in sperm. (**L**) Comparison of Slo3 current amplitude at +100 mV before NH_4Cl application between control (152.4 ± 25.05 pA; n=6) and in the presence of 100 µM ZnPy (187.5 ± 79.53 pA; n=4), p=0.4862, Welch's t-test. (**M**) Comparison of Slo3 current amplitude at +100 mV after NH_4Cl application between control (427.6 ± 88.28 pA; n=4) and in the presence of 100 µM ZnPy (249.2 ± 130.6 pA; n=4), p=0.0703, Welch's t-test. (**N**) Comparison of the fold change in Slo3 current amplitude at +100 mV after NH_4Cl application between control (2.39 ± 0.55; n=4) and in the presence of 100 µM ZnPy (1.4 ± 0.56; n= 4), p=0.0465, Welch's t-test. All error bars are ± SD centered on the mean.

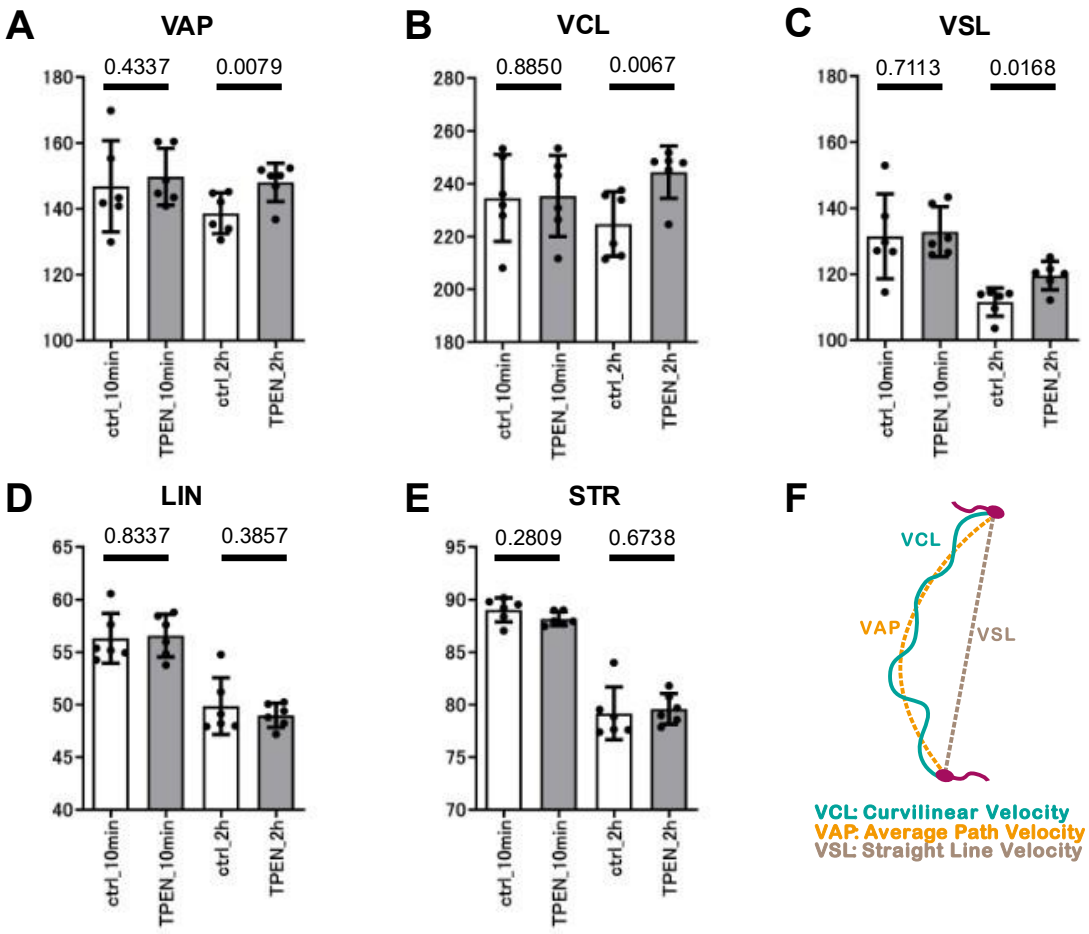

Figure 1—figure supplement 1. Effects of intracellular zinc on sperm motility before and after capacitation. Comparison of VAP, VCL and VSL show that intracellular zinc affects these kinds of motions only after the sperm underwent capacitation. (**A-E**) Quantitation of sperm motility parameters at: 10 min (control); 10 min in the presence of zinc chelator TPEN; 2 h after TYH incubation, a well-established capacitation-inducing medium (control); and 2 h after THY incubation in the presence of TPEN. Bar graph shows the comparison of (**A**) VAP (average path velocity); (**B**) VCL (curvilinear velocity); (**C**) VSL (straight-line velocity); (**D**) STR (straightness); and (**E**) LIN (linearity) as depicted in (**F**). All error bars are ± SD centered on the mean.

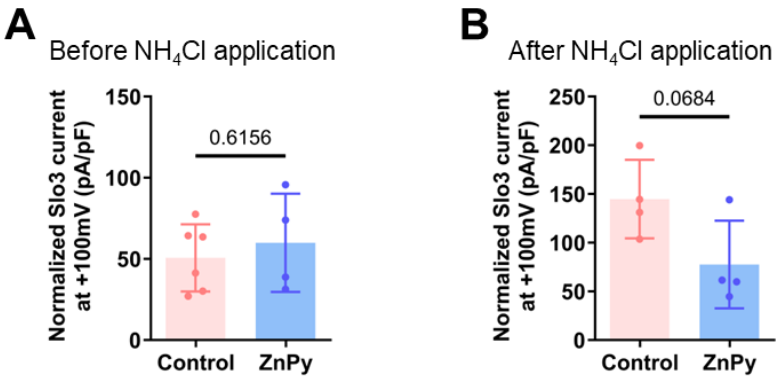

Figure 1—figure supplement 2. The effects of zinc on Slo3 current in sperm cells. (**A**) Comparison of normalized Slo3 current at +100 mV before NH_4Cl application between control (50.67 ± 20.67 pA/pF; n=6) and in the presence of 100 µM ZnPy (59.95 ± 30.24pA/pF; n= 4), p=0.6156, Welch's t-test. (**B**) Comparison of normalized Slo3 current at +100 mV after NH_4Cl application between control (144.8 ± 40.36 pA/pF) and in the presence of 100 µM ZnPy (77.59 ± 44.97pA/pF; n= 4), p=0.0684, Welch's t-test. All error bars are ± SD. centered on the mean.

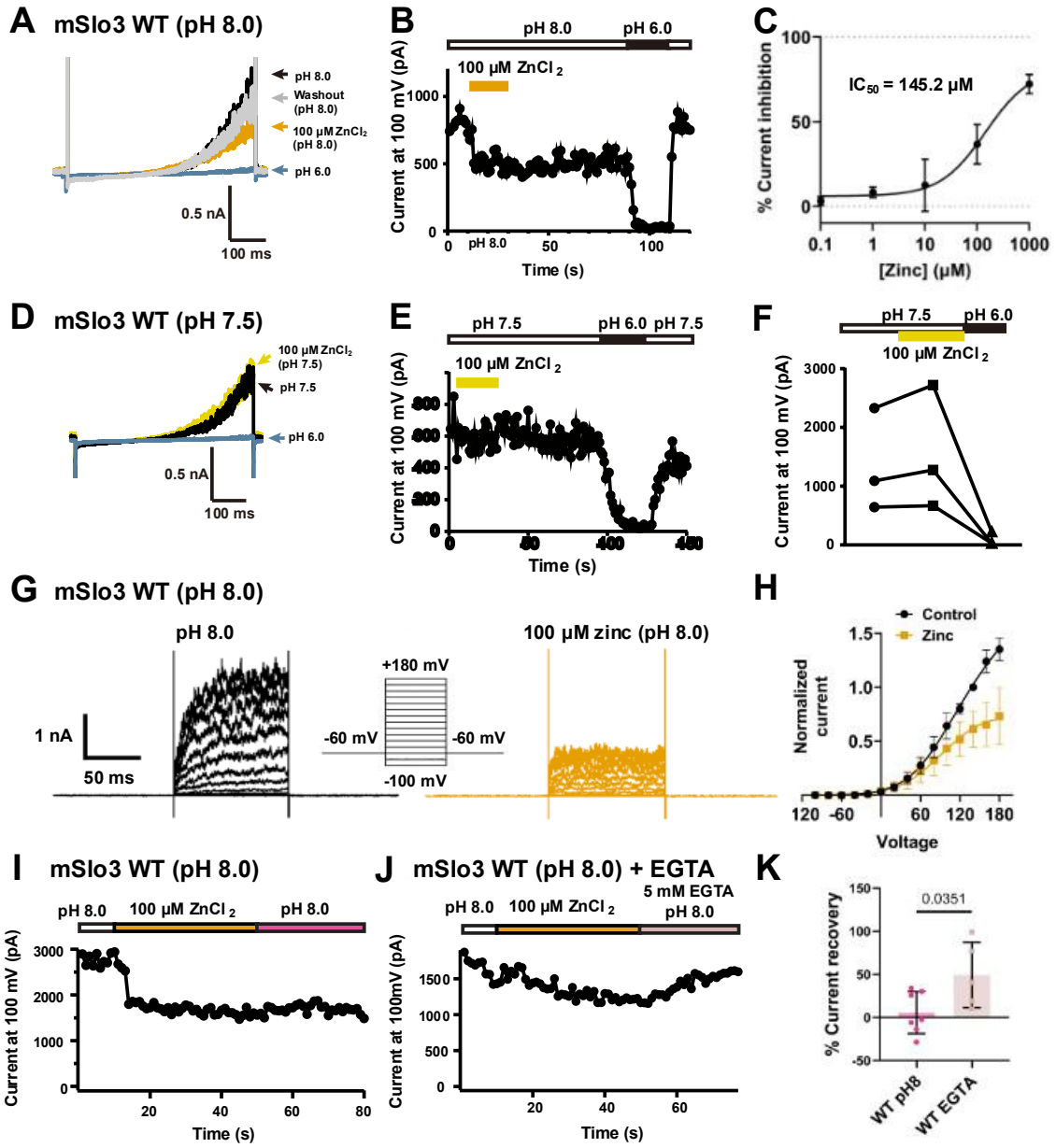

Figure 2. Zinc inhibits mouse Slo3 (mSlo3) current. (**A-C**) Inside-out patch-clamp recording of mSlo3 with pHi=8.0 by applying ramp pulse from -100 mV to +100 mV with the holding potential of 0 mV**.** (**A**) Representative current traces upon the application of pH 8.0 (black); 100 μM of zinc in pH 8.0 (yellow orange); pH 6.0 (blue); and wash-out by pH 8.0 (gray) after pH 6.0. (**B**) Time course of the change in current amplitude at +100 mV in response to pH 8.0, 100 μM zinc, pH 6.0, and pH 8.0 as indicated (white: pH 8.0; yellow orange: 100 μM zinc in pH 8.0; solid black: pH 6.0). (**C**) Dose-response curve of zinc inhibition in mSlo3 current (pH 8.0). % current inhibition was plotted assuming that the dose response curve has a standard slope, equal to a Hill slope of -

1.0. IC_{50} = 145.2 μM; n = 2-6. (**D-F**) Inside-out patch-clamp recording of mSlo3 in *Xenopus* oocyte with pHi=7.5 by applying ramp pulse from –100 mV to +100 mV with the holding potential of 0 mV**.** (**D**) Representative current traces upon the application of pH 7.5 (black); μM of zinc (yellow); and pH 6.0 (blue). (**E**) Time course of the change in current amplitude at +100 mV in response to pH 7.5, 100 μM zinc, and pH 6.0 as indicated (white: pH 7.5; yellow: 100 μM zinc in pH 7.5; solid black: pH 6.0). (**F**) Current amplitude at +100 mV upon the application of pH 7.5, 100 μM zinc in pH 7.5, and pH 6.0 from individual cell, as indicated. (**G-H**) Inside-out patch-clamp recording of mSlo3 with pHi=8.0 by applying step pulses from –100 mV to +180 mV with the holding potential of -60 mV**.** Zinc inhibition is voltage-dependent. (**G**) Representative current traces upon the application of pH 8.0 (black) and 100 μM of zinc in pH 8.0 (yellow orange). (**H**) I-V relationship of control (pH 8.0; black) and zinc (100 μM; yellow orange). Normalization was performed by dividing the absolute current of mSlo3 at pH 8.0 of each voltage by the absolute current at the pre-determined highest voltage that still produced a stable mSlo3 current (i.e., good patch, good clamp). In this analysis, +140 mV was chosen as the highest voltage for normalization, since in few cells the patch was lost at +160mV and +180mV. Similar to the control condition, the absolute current of mSlo3 in the presence of 100 μM zinc was normalized to the absolute current of the control at +140 mV. I-V curve was fitted by Boltzmann equation for control and followed by Woodhull equation for zinc inhibition ($V_{50\ Ctrl}$ = 85.24; Slope $_{Ctrl}$ = 35.51; V_{block} Zn = 188.8; $Slope_{block}$ Zn = -115.3; n=13). (**I-K**) Inside-out patch-clamp recording of mSlo3 with the application of 5 mM EGTA in pH=8.0 by applying ramp pulse from –100 mV to +100 mV with the holding potential of 0 mV. Zinc has a long-lasting inhibitory effect on mSlo3, and it could be rescued by EGTA (**I**) Time course of the change in current amplitude at +100 mV in response to pH 8.0, 100 μM zinc, and pH 8.0 as indicated (white: pH 8.0; yellow orange: 100 μM zinc in pH 8.0; pink: pH 8.0 for wash-out). (**J**) Time course of the change in current amplitude at +100 mV in response to pH 8.0, 100 μM zinc, and 5 mM EGTA in pH 8.0 as indicated (white: pH 8.0; yellow orange: 100 μM zinc in pH 8.0; light lilac: 5 mM EGTA in pH 8.0 for wash-out). (**K**) Comparison of percentage of current recovery between pH 8.0 only (5.62 ± 24.40 %; n= 7) and 5 mM EGTA in pH 8.0 (49.22 ± 37.98 %; n=5), p=0.0351, unpaired t-test. All error bars are ± SD centered on the mean.

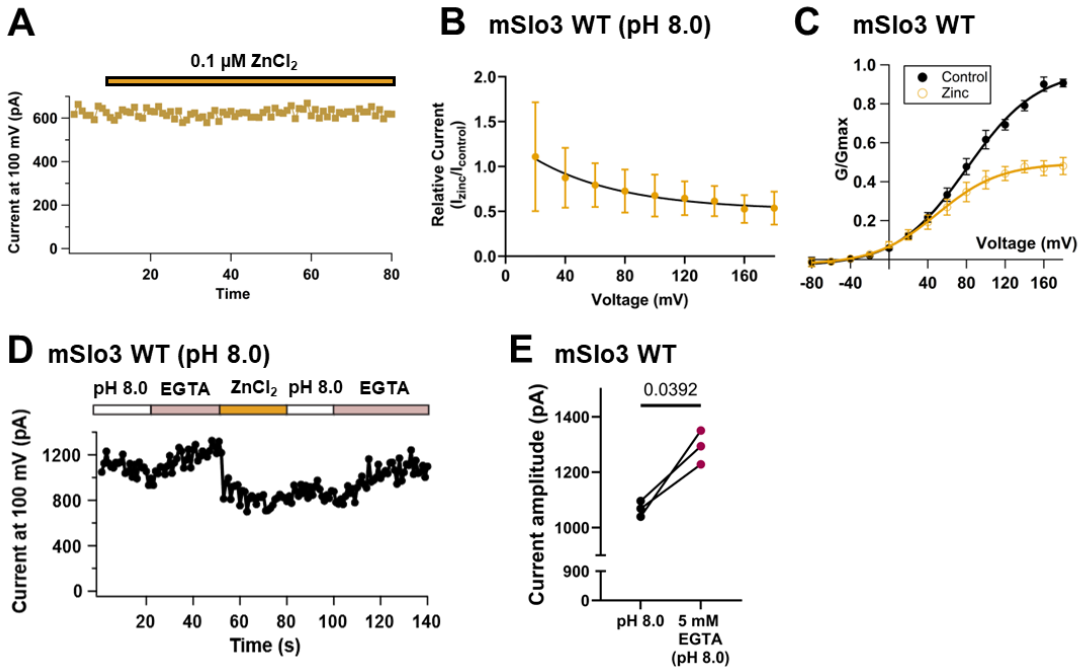

Figure 2—figure supplement 1. Zinc inhibits mSlo3 current. (**A**) Time course of Slo3 current at + 100 mV upon the application of 0.1 μM zinc. (**B**) Relationship between relative current ($I_{zinc}/I_{control}$) with membrane voltage at pH 8.0 shows that zinc inhibits mSlo3 current in voltage-dependent manner. (**C**) G-V relationship comparison of mSlo3 current between control (pH 8.0; black filled circle) and upon the application of 100 μM zinc in pH 8.0 (yellow orange circle) (V_{50} control = 80.67 ± 2.32; V_{50} zinc = 49.677 ± 1.38; n=13). Normalization was done based on the maximum conductance in control. (**D**) Time course of the change in current amplitude at +100 mV in response to pH 8.0, 5 mM EGTA in pH 8.0, 100 μM zinc, pH 8.0, and 5 mM EGTA in pH 8.0 as indicated (white: pH 8.0; yellow orange: 100 μM zinc in pH 8.0; pale lilac: 5 mM EGTA in pH 8.0). The baseline current showed a slight increase upon perfusing with 5 mM EGTA, indicating that endogenous zinc is already present in mSlo3, and it is affecting the baseline current. (**E**) Comparison of percentage of mSlo3 current evoked by pH 8.0 and 5 mM EGTA in pH 8.0 (p=0.0392). Statistical analysis was done by paired t-test, n=3. All error bars are ± SD centered on the mean.

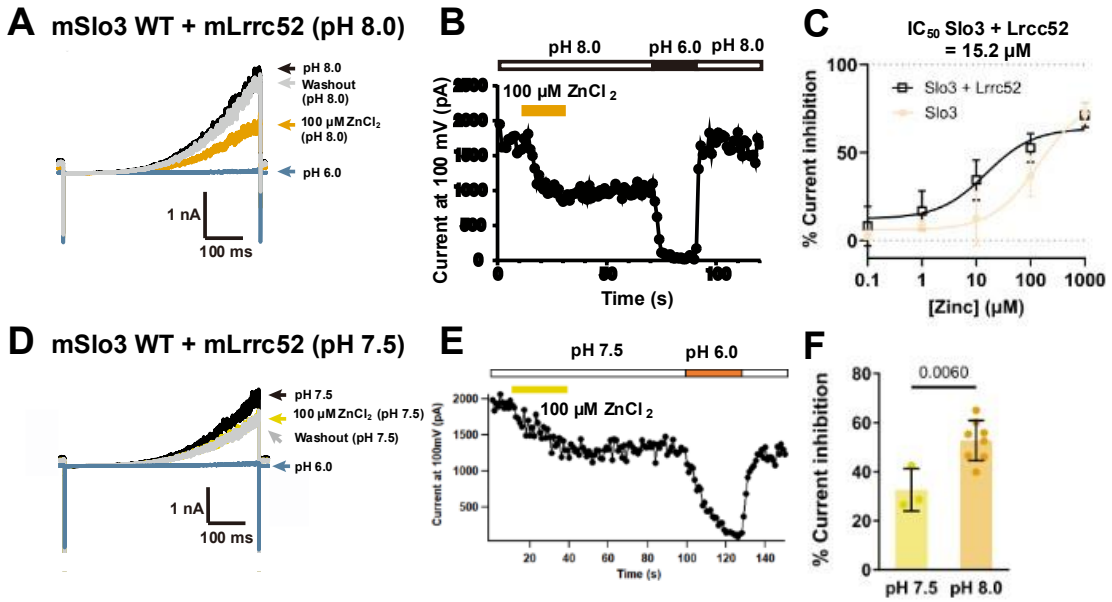

Figure 3. Zinc inhibits mSlo3 current when co-expressed with gamma subunit Lrrc52. (**A-B**) Inside-out patch-clamp recording of mSlo3 co-expressed with mLrrc52 with pHi=8.0 by applying ramp pulse from –100 mV to +100 mV with the holding potential of 0 mV**.** (**A**) Representative current traces upon the application of pH 8.0 (black); 100 μM of zinc in pH 8.0 (yellow orange); pH 6.0 (blue); and wash-out by pH 8.0 after pH 6.0 (gray). (**B**) Time course of the change in current amplitude at +100 mV in response to pH 8.0, 100 μM zinc, pH 6.0, and pH 8.0 as indicated (white: pH 8.0; yellow orange: 100 μM zinc in pH 8.0; solid black: pH 6.0). (**C**) Dose-response curve of zinc inhibition in mSlo3 co-expressed with mLrrc52 current (pH 8.0). % current inhibition was plotted assuming that the dose response curve has a standard slope, equal to a Hill slope of -1.0. IC_{50} = 15.2 μM; n = 3-8. (**D-E**) Inside-out patch-clamp recording of mSlo3 in *Xenopus* oocyte co-expressed with mouse Lrrc52 (mLrrc52) with pHi=7.5 by applying ramp pulse from –100 mV to +100 mV with the holding potential of 0 mV**.** (**D**) Representative current traces upon the application of pH 7.5 (black); μM of zinc (yellow); pH 7.5 for wash-out (grey); and pH 6.0 (blue). (**E**) Time course of the change in current amplitude at +100 mV in response to pH 7.5, 100 μM zinc, pH 6.0, and pH 7.5 for wash-out as indicated (white: pH 7.5; yellow: 100 μM zinc in pH 7.5; orange pH 6.0). (**F**) Comparison of the percentage of current inhibition by 100 μM zinc between pH 7.5 (32.51 ± 8.62 %; n=3) and pH 8.0 (52.61 ± 8.23 %; n=8), p=0.006; unpaired t-test. All error bars are ± SD centered on the mean.

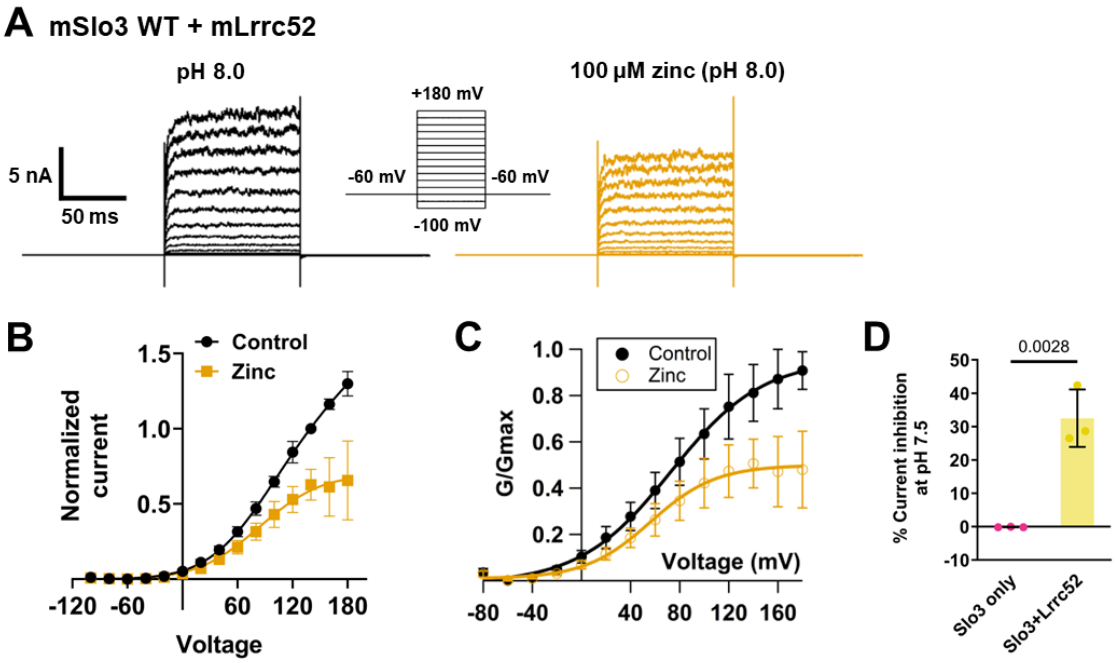

Figure 3—figure supplement 1. Zinc inhibits mSlo3 current when coexpressed with auxiliary Lrrc52. (**A-C**) Inside-out patch-clamp recording of mSlo3 co-expressed with mLrrc52 with pHi=8.0 by applying step pulses from –100 mV to +180 mV with the holding potential of -60 mV**.** Zinc inhibition is voltage-dependent. (**A**) Representative current traces upon the application of pH 8.0 (black) and 100 μM of zinc in pH 8.0 (yellow orange). (**B**) I-V relationship of control (pH 8.0; black) and zinc (100 μM; yellow orange). I-V curve was fitted by Boltzmann equation for control and followed by Woodhull equation for zinc inhibition ($V_{50\ Ctrl}$ = 74.01; Slope $_{Ctrl}$ = 36.47; V_{block} Zn = 185.5; $Slope_{block}$ Zn = -130.4; n=8). (**C**) G-V relationship comparison of mSlo3 current co-expressed with mLrrc52 between control (pH 8.0; black filled circle) and upon the application of 100 μM zinc in pH 8.0 (yellow orange circle) (n = 13). V_{50} control = 72.93 ± 2.06 V_{50} zinc = 56.22 ± 2.75. Normalization was done based on the maximum conductance in control. (**D**) Comparison of the percentage of Slo3 current inhibition at pH 7.5 between Slo3 only (-0.13 ± 0.08 %; n=3) and Slo3+Lrrc52 (32.51 ± 8.62 %; n=3), p=0.0028, unpaired t=test. All error bars are ± SD centered on the mean.

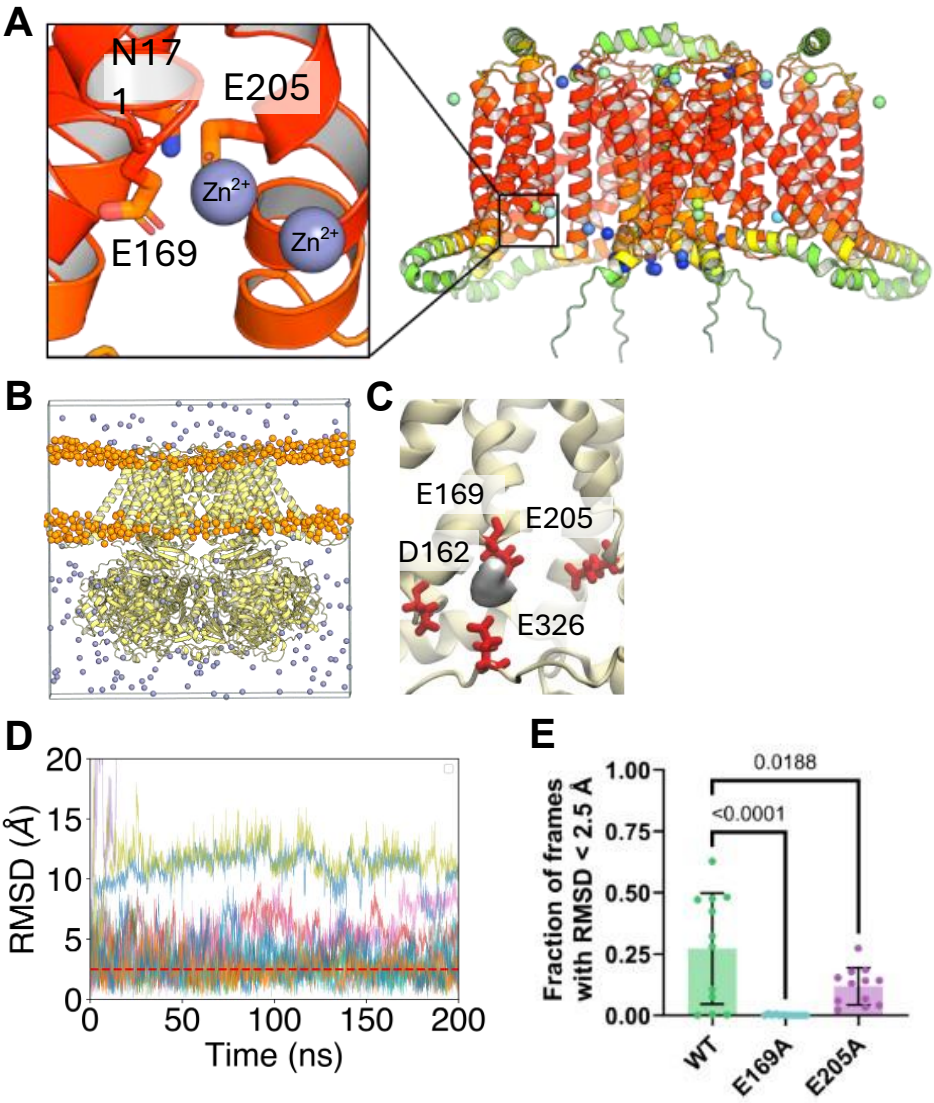

Figure 4. Computational studies show that the Zn binding site on mSlo3 is located near E169 and E205. (**A**) AlphaFold3 prediction of the Zn binding site on the transmembrane segment of the Slo3 channel. Zn is shown as grey spheres, and Slo3 is shown using an orange cartoon. (**B**) The system is set up for flooding simulations. The phosphorus atoms on the POPC lipid are shown in orange. All Zn ions in the system are shown as grey spheres. The Slo3 channel is shown in the yellow cartoon. All water, KCl and other atoms within POPC molecules are omitted for clarity. (**C**) The density of Zn ions within 4 Å of the protein molecules was calculated using VolMap averaged across 200 ns flooding simulations (n = 3). Key acidic contacting residues are shown as red sticks. (**D**) Root mean square (RMSD) calculation of the 12 Zn ions fitted to the C alpha atoms of the protein on the first frame for 200 ns. Given that there are 4 Zn in each subunit per repeat, this

leads to 12 data sets shown in different colored plots. The red dotted line marked the cutoff at 2.5 Å. (**E**) The fractions of frames where the RMSD of zinc ions are less than 2.5 Å in WT channel, E169A and E205A mutants ($p<0.0001$, $p=0.0188$, respectively). Statistical analysis was done by one-way ANOVA with Dunnett's post-hoc test compared to the WT group for each mutant ($n=12$). All error bars are ± SD centered on the mean.

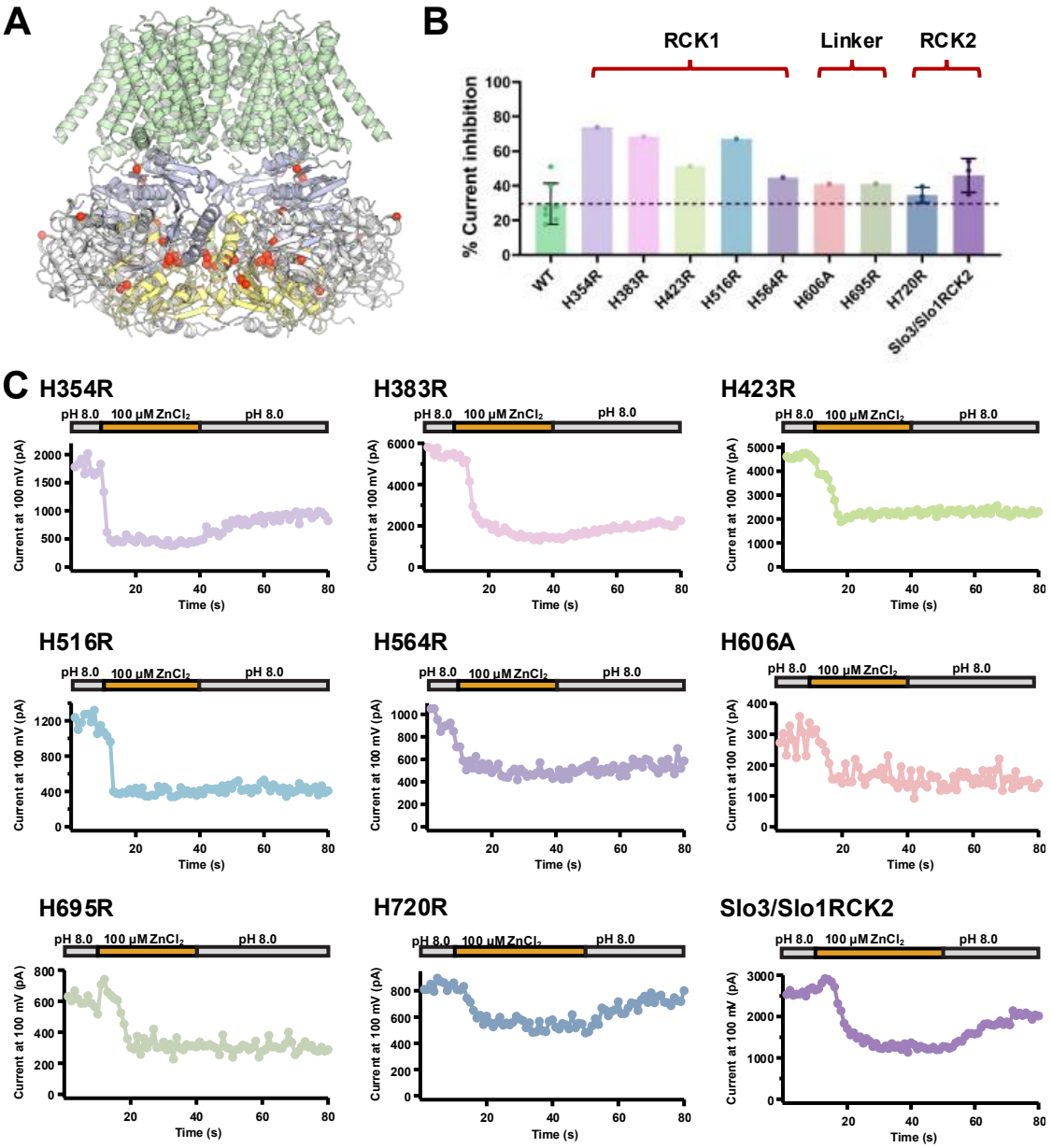

Figure 4—figure supplement 1. Computational studies and scanning mutagenesis of zinc binding site in mSlo3 channel. (**A**) The full-length Slo3 tetramer structure predicted by AlphaFold3, with RCK1 and RCK2 represented in blue and yellow cartoons, respectively, and 50 Zn^{2+} ions depicted as red spheres.(**B**) Comparison of the percent current inhibition upon the application of 100 μM zinc between wildtype and all the histidine mutants scanned (histidine residues located in RCK1, RCK1/RCK2 linker, RCK2, and the chimera in which the RCK2 of mSlo3 is replace with the RCK2 from mSlo1). Dotted black line indicates mean of control (WT).

(**C**) Time course of the change in current amplitude at +100 mV in response to pH 8.0, 100 μM zinc, and pH 8.0 for wash-out as indicated for all the mutants as stated. All error bars are ± SD centered on the mean.

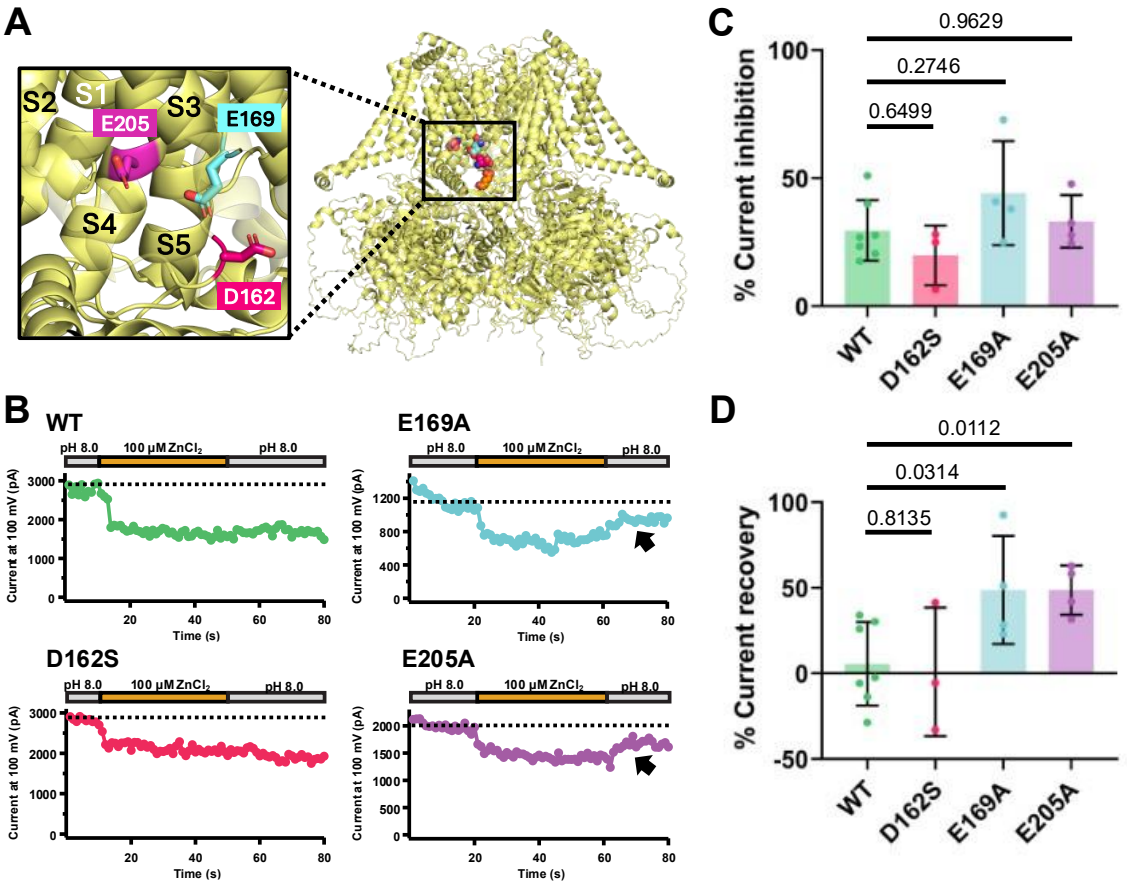

Figure 5. E169 and E205 located within VSD are important for the sustained zinc inhibition of mSlo3 current. (**A**) Tetrameric mSlo3 structure representation. Inset shows rotated view of selected region which indicates predicted zinc binding site from MD simulations located within the voltage-sensor domain: D162 (S2-S3 linker), E169 (S3 domain), and E205 (S4 domain) which have been mutated to elucidate the zinc binding site in mSlo3. mSlo3 structure representation in (**A**) was based on structure prediction using AlphaFold3 (Abramson et al., 2024), mSlo3 sequence was retrieved from NCBI NP_032458.3. Some portions of the S2 and S3 domains have been rendered highly transparent to enhance clarity. (**B**) Time course of the change in current amplitude at +100 mV in response to pH 8.0, 100 μM zinc, and pH 8.0 for wash-out as indicated for: WT, D162S, E169A, and E205A. The dotted line indicated the level of activated mSlo3 current at pH 8.0. Black arrows indicated the current recovery observed upon wash-out. (**C**) Comparison of the percent current inhibition upon the application of 100 μM zinc between WT, D162S, E169A, and E205A (p=0.6499, p=0.2746, p=0.9629, respectively). Statistical analysis was done by one-way ANOVA with Dunnett's post-hoc test compared to the control group (WT), n=3-7 (**D**) Comparison of

percentage of current recovery upon wash-out using pH 8.0 between WT, D162S, E169A, and E205A ($p=0.8135$, $p=0.0314$, $p=0.0112$, respectively). Statistical analysis was done by unpaired t-test compared to the WT group for each mutant, $n=3$-7. All error bars are ± SD centered on the mean.

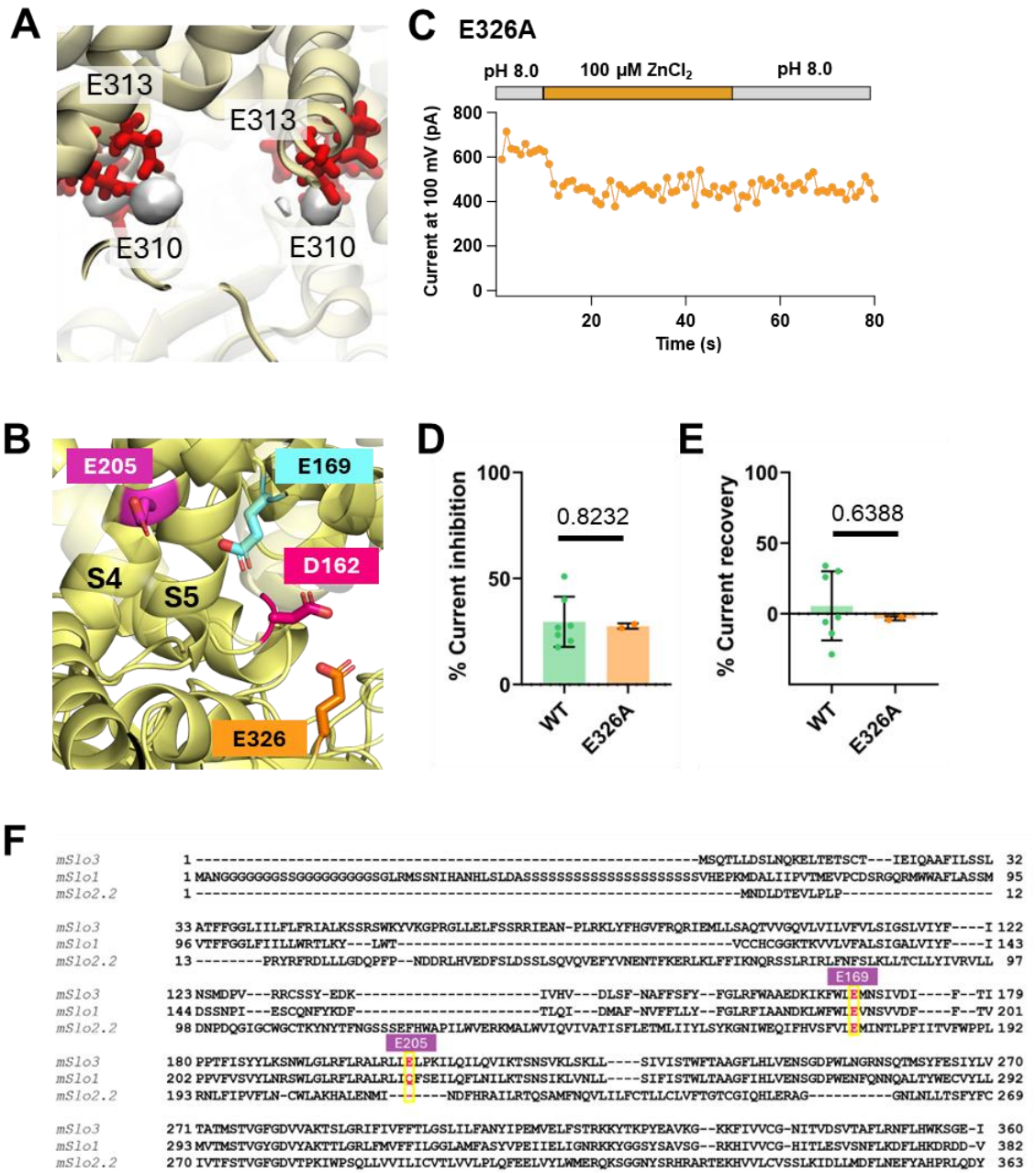

Figure 5—figure supplement 1. Computational studies and mutagenesis of zinc binding site in mSlo3 channel. (**A**) The density of Zn ions within 4 Å of the protein molecules was calculated using VolMap averaged across 200 ns flooding simulations (n = 3). Key acidic contacting residues are shown as red sticks. (**B**) Tetrameric mSlo3 structure representation of selected region which indicates D162 (S2-S3 linker), E169 (S3 domain), E205 (S4 domain), and E326 (intracellular linker between TM and RCK1) which have been mutated to elucidate the zinc binding site in mSlo3. (**C**) Time course of the change in current amplitude at +100 mV in response to pH 8.0, 100 μM zinc,

and pH 8.0 for wash-out as indicated for E326A. (**D**) Comparison of the percent current inhibition upon the application of 100 μM zinc between wildtype and E326A (p=0.8232, unpaired t-test, n=2-7). (**E**) Comparison of percentage of current recovery upon wash-out using pH 8.0 between WT and E326A (p=0.6388, unpaired t-test, n=2-7). All error bars are ± SD centered on the mean. (**F**) Sequence alignment of mSlo3 (NP_032458.3), mSlo1 (NP_001240293.1) and mSlo2.2 (NP_001138875.1) using ClustalO. E169 and E205 residues (mslo3 numbering) are highlighted in red text with a yellow box.

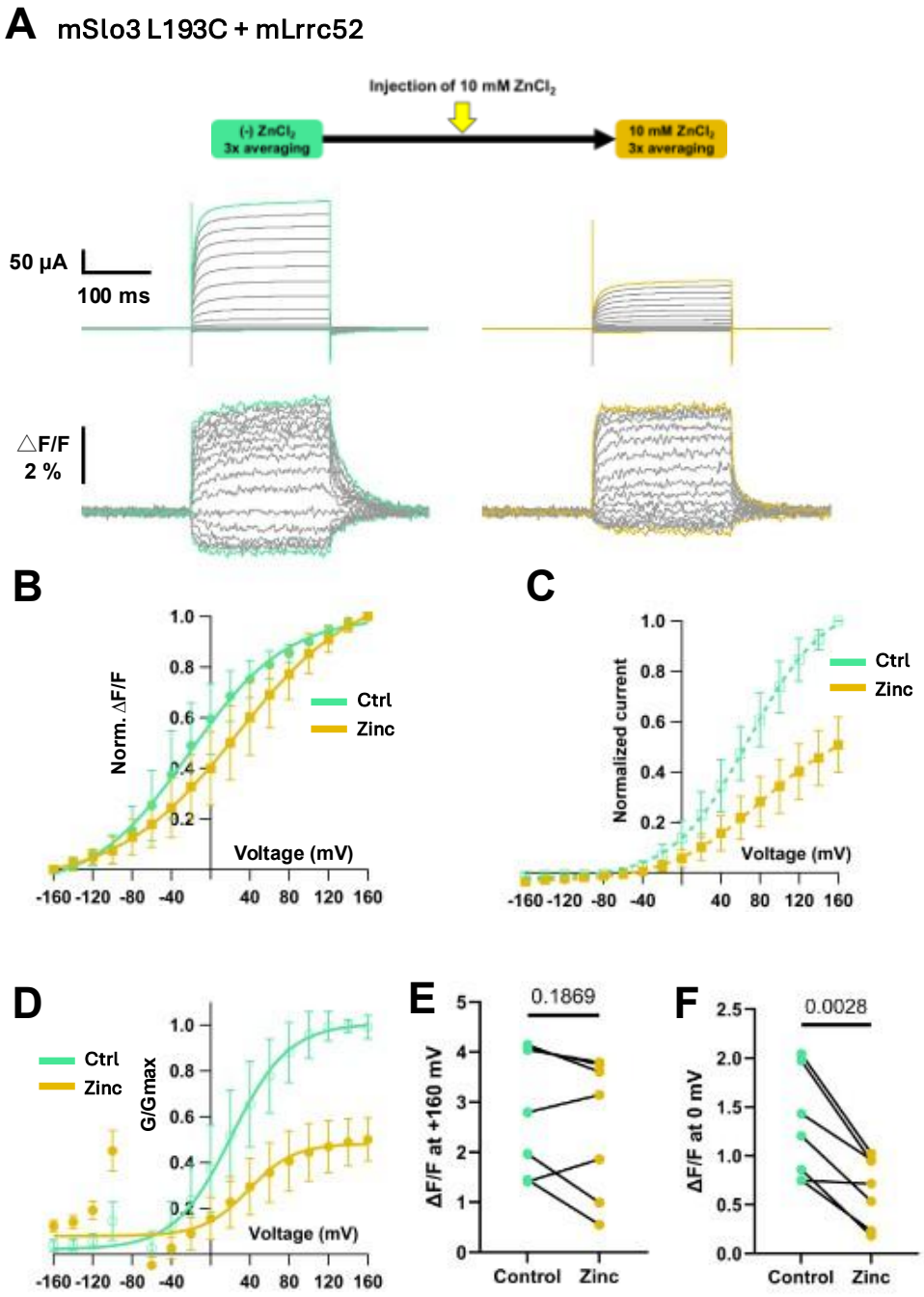

Figure 6. Zinc influenced the motion of the voltage-sensing domain (VSD) of mSlo3 channel. (**A**) Representative current traces and fluorescence signals of mSlo3 L193C coexpressed with Lrrc52 in the absence (green) and presence (yellow orange) of zinc. The inset illustrates a schematic timeline of direct zinc injection using a glass needle and positive pressure. Voltage steps from -160 mV to + 160 mV were applied with a holding potential of -60 mV. Zinc was injected into the same

cell after the initial VCF recording (green), followed by a second VCF recording 60 seconds post-injection (yellow orange). $\Delta F/F_{Control}$ = 2.84 ± 1.25 % (n=7); $\Delta F/F_{Zinc}$ = 2.53 ± 1.37 % (n=7). The green and yellow orange traces represent the current and fluorescence signals at in +160 mV and -160 mV, in the absence (green) and presence (yellow orange) of zinc. (**B**) Comparison of the F-V relationship between control (green) and zinc (yellow orange). The F-V curve was fitted using Boltzmann equation (V_{50} control = =-21.68 ± 3.04; V_{50} zinc = =27.04 ± 1.05; n=7). Normalization was done based on the maximum ΔF/F for each control and zinc-injected conditions. (**C**) I-V relationship showing inhibition of mSlo3 L193C+Lrrc52 currents by direct zinc injection. Traces compare control (green) and zinc (yellow orange). (**D**) G-V relationship comparison of mSlo3 L193C current co-expressed with mLrrc52 between control (green circle) and zinc-injected (yellow orange circle) conditions (V_{50} control = 21.11 ± 4.8; V_{50} zinc = 38.62 ± 28.8; n=7). Normalization was done based on the maximum conductance in control. (**E**) Comparison of ΔF/F in the absence and presence of zinc at +160 mV from the same cell (p=0.1869, paired t-test, n=7). (**F**) Comparison of ΔF/F in the absence and presence of zinc at 0 mV from the same cell (p=0.0028, paired t-test, n=7). All error bars are ± SD centered on the mean.

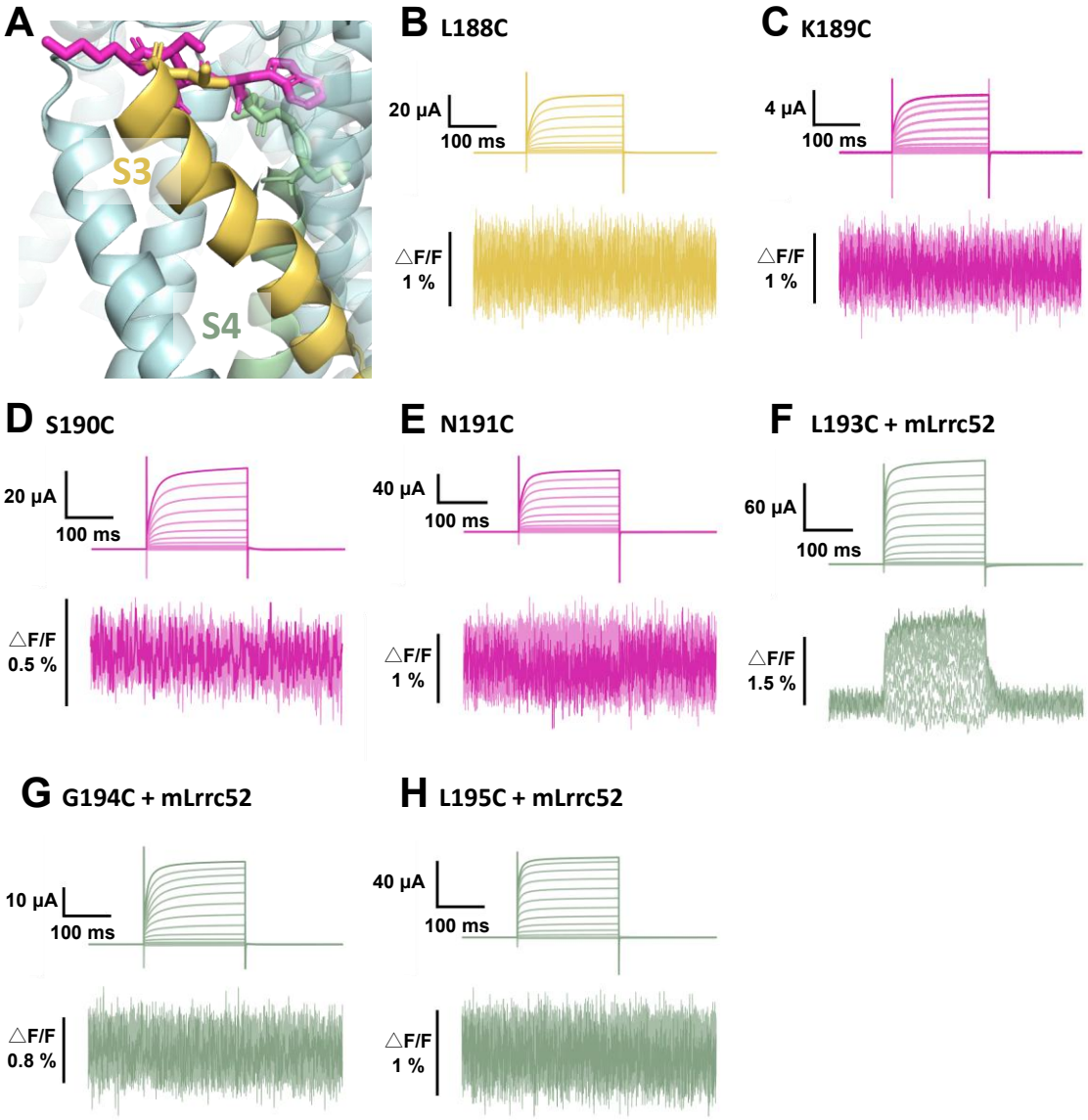

Figure 6—figure supplement 1. Scanning mutagenesis of mSlo3 channel VCF construct. (**A**) Structural representation of the VCF scanning regions in the mSlo3 channel, highlighting the top of S3 (yellow), the S3-S4 linker (violet), and the top of S4 (mud green). (**B-H**) Representative current traces and fluorescence signals recorded upon voltage steps from -80 mV to +160 mV with a holding potential of -60 mV for L188C, K189C, S190C, N191C, L193C (+mLrrc52), G194C (+mLrrc52), and L195C (+mLrrc52), respectively (n=4-7; ΔF/F mSlo3 L193C+Lrrc52: = 1.15 ± 0.48 % [n = 4]).